Friedrich-Alexander-Universität
Naturwissenschaftliche Fakultät

Bachelor Thesis
in Physics

Finite element analysis of a KM3NeT optical module

Oliver Plathner

Supervisor: apl. Prof. Dr. Robert Lahmann

Erlangen Centre for Astroparticle Physics

Submission date: 14.07.2025

Abstract

Neutrino detection in the deep sea relies on the detection of Cherenkov radiation, produced by charged elementary particles, occurring as a product of neutrino interactions. In the KM3NeT deep-sea neutrino detector, photomultiplier tubes are housed inside glass spheres, which are often referred to as digital optical modules (DOMs). These DOMs are anchored to the seabed, experiencing slight movements because of varying ocean currents. To determine their positions in real time, an acoustic positioning system is employed, which uses beacons on the seafloor and piezoelectric sensors glued to the inside of the DOM shells. However, the current positioning algorithms neglect the propagation of the acoustic positioning signals through the glass shell, which could introduce systematic errors. Experimental findings from the modified AMADEUS project revealed the glass waves to resemble two *Lamb-like* modes of zeroth order, traveling faster than the speed of sound in the water around the detector. Building upon this experiment, this study utilizes finite element simulations to analyze elastic waves propagating through glass of different shapes. These simulations strengthen the assumption of dispersive Lamb-like wave modes and enable a measurement method of their propagation speeds through the DOM shell. The findings of this work provide a path for the correction of systematic positioning errors in the KM3NeT localization system, improving the accuracy of neutrino detection in the deep sea.

Contents

1 Introduction **3**

2 KM3NeT and ANTARES **4**
2.1 Technical aspects of KM3NeT 4
2.2 The positioning system 5

3 Lamb waves **8**
3.1 The free plate problem 8
3.2 Application of the free plate problem 12

4 Finite Element Method (FEM) **13**
4.1 Governing equations 13
4.2 Discretization 13
4.3 The weak formulation 15
4.4 Solution 15
4.5 Sources of error in FEM 16

5 Simulations **17**
5.1 Simulation 1: Glass plate 17
5.1.1 Simulation setup 17
5.1.2 Simulation results 21
5.2 Simulation 2: Glass spherical shell 26
5.2.1 Simulation setup 26
5.2.2 Simulation results 27

6 Summary and conclusions **35**

A Simulation history **36**
A.1 Glass Plate 36
A.2 DOM geometry 41

B Modeling instructions **42**
B.1 Glass plate 42
B.2 DOM geometry 46

C Material properties **50**

D Figures **50**

1 Introduction

Traditionally, astronomical events are analyzed with the detection of photons, emitted by these events. Photons are excellent carriers of information because they are not affected by electromagnetic fields, meaning they can travel through space without disturbance of their original trajectory. In astronomy, this property is crucial, as otherwise the detected photons cannot be traced back to their original source. In addition to directional information, photons carry energy, which is utilized to classify the observed events.
Since the first observation of neutrinos in the Cowan-Reines-neutrino-experiment, the pursuit of detecting cosmic neutrinos has become a major objective in astrophysics. Today, neutrino astronomy is an independent field of astronomy, with numerous experiments and international collaborations, offering new insights on cosmic events.
Neutrinos are well-suited for astronomical observations, as they are the only known particles to interact via the weak force exclusively. This not only allows them to travel through space without deflection by electromagnetic fields like photons, but makes them extremely penetrating, meaning they rarely interact with matter. These characteristics make them ideal messengers of astrophysical processes, analogously to traditional photon driven methods.
Due to the penetrating nature of neutrinos, the detection is a technical challenge and usually vast detection volumes need to be monitored for neutrino interactions. A widely used detection method is the observation of Cherenkov radiation, which is emitted by charged particles produced by a neutrino-matter interaction. This light is typically detected by photomultiplier tubes (PMTs), and can be utilized to reconstruct trajectory and energy information of the original neutrino.
Since Cherenkov-radiation is absorbed by most materials, the neutrino interaction has to happen in an optically transparent medium, such as ice or water. Neutrino telescopes, detecting Cherenkov radiation in seawater are called deep-sea-neutrino telescopes. Two examples for such telescopes are the KM3NeT-telescope [9] network and its predecessor ANTARES [8]. Both of these telescopes work by detecting Cherenkov-radiation with the help of PMTs, spaced across large detection volumes deep in the mediterrenian sea. The PMTs are embedded in so called optical modules (OMs), which are pressure resistant glass spheres and are distributed across lines vertical to the sea floor with no fixed location, moving with underwater currents. To correctly reconstruct a neutrino event, it is crucial to locate the optical modules accurately.
Both KM3NeT and ANTARES rely on an acoustic positioning system to determine the location of their OMs. While these systems are already precise, tests with the AMADEUS [6] system demonstrated potential for an immediate improvement of the positioning accuracy for the ANTARES telescope. In this thesis a similar analysis inspired by the AMADEUS experiment is conducted for KM3NeT, with the aim of improving its positioning system. As the construction of an experimental test setup would be costly and time-inefficient, the analysis is done with a simulation by the method of finite elements (FEM).
Section 2 introduces the KM3NeT and ANTARES neutrino telescopes as well as the AMADEUS setup, describing their technical details. Section 3 discusses the theory of ultrasonic elastic waves in solid media and their importance for this topic. In section 4, a short, theoretical introduction to the method of finite elements is given, before the simulation setups as well as their results are discussed in section 5. Section 6 summarizes the important insights of this analysis.

2 KM3NeT and ANTARES

KM3NeT is an observatory for high-energy neutrinos, consisting of multiple detection sites located in the deep Mediterranean sea ($\sim$ 3000 m below the surface). This depth provides shielding from other cosmic-ray-induced background particles, such as muons, of which only few will reach such depths. The name stands for *Cubic Kilometer (km^3) Neutrino Telescope*, as large detection volumes are necessary for the detection of high-energy neutrino events.
The predecessor of the currently under-construction KM3NeT-network is called ANTARES, an earlier experimental deep-sea neutrino telescope. However, it is smaller, as its intended purpose was to prove the feasibility of this type of neutrino detector, which it successfully accomplished during its time of operation between 2006 and 2022 [8].
The core detection principle of both KM3NeT and ANTARES relies on observing Cherenkov-radiation, which is emitted by charged secondary particles from the neutrino interactions occurring in and around the detector [8]. This radiation is detected with photomultiplier tubes, housed inside of pressure-resistant glass spheres, referred to as **digital optical modules** (DOMs), seen in figure 1.
The DOMs are installed across multiple lines vertical to the sea floor and are localized via acoustic multilateration. By analyzing the amount and arrival times of the Cherenkov photons, the direction, flavor and energy of the neutrino can be inferred. Because neutrinos are not deflected in space, their reconstructed trajectories can be traced back to their astrophysical source [8].
During the operational period of ANTARES, an additional system named AMADEUS was implemented to explore alternative detection methods. AMADEUS tested the feasibility of acoustic neutrino detection, based on the pressure waves generated by localized heating of water from energy deposition during a neutrino interaction [20]. The setup and methodology are detailed in [20]. For this thesis, it is important to note that the AMADEUS system was later modified to analyze signal propagation in the glass housing, with results published in [6].

2.1 Technical aspects of KM3NeT

As described, the primary components of the set-up are DOMs arranged on strings attached to the sea floor. DOMs are spherical pressure vessels made of Vitrovex glass, with an outer diameter of $d_o = 432$mm and a minimal thickness of $15mm$, which are capable of withstanding the pressure at depths up to $6700m$ [11]. Inside each KM3NeT-DOM, 31 small PMTs with photodiode diameters of 72mm are mounted [9]. These PMTs are responsible for detecting the Cherenkov photons. Of particular interest for this thesis is the piezoelectric acoustic sensor glued to the inside of the shell, which detects the acoustic positioning signals.
Additional components include a compass and a tilt meter, for orientation measurements, as well as LEDs for calibration purposes [9]. The rest of the module is occupied with control and readout electronics.
These DOMs are connected vertically along two parallel ropes to form a detection string, or detection unit (DU) as illustrated in figure 1.

Figure 1: A close up photograph of a DOM (right). The circular cutouts are where the PMTs are positioned inside the DOM. The central white spot is the acoustic piezo sensor. Schematic view of a detection string (left), with the yellow ball at the top being the buoy.

The KM3NeT telescope network is compromised of two sites, called KM3NeT/ARCA (Astroparticle Research with Cosmics in the Abyss) and KM3NeT/ORCA(Oscillation Research with Cosmics in the Abyss). As their experimental goals, described in [9], are different, the geometry of the DUs is optimized for each site [9]. For ARCA, the strings are 700m long and the distance between the DOMs is 36m with the first being 80m of the sea floor. For ORCA, the strings have a length of 200m, with the DOMs spaced 9m apart, with the first DOM 40m above sea floor. Horizontally, the strings are spaced about 95m apart, for the ARCA configuration and about 20m for ORCA [9].
The strings are anchored to the sea floor and tensioned by buoys attached at the upper end of the string as seen in figure 1. The power and data transmission lines are connected to a junction box, which relays signals through a main transmission line to the onshore station, which hosts the data acquisition electronics and a PC farm for data filtering [9]. The full detector consists of large arrays of these strings as illustrated in figure 2.

2.2 The positioning system

To accurately reconstruct the tracks of neutrino-induced particles and, in turn, the trajectory of the neutrino, the positions of the DOMs must be tracked with an accuracy of $\pm$10cm. This is achieved using an acoustic multilateration system, which updates the DOMs positions several times per minute, depending on sea current activity [13].
This system compromises acoustic transmitters (beacons) positioned on the sea floor at known locations outside the footprint of the telescope, as well as digital acoustic receivers built into the DOMs. The beacons are placed outside the array footprint to improve triangulation geometry, especially for DUs near the edges of the detector volume.

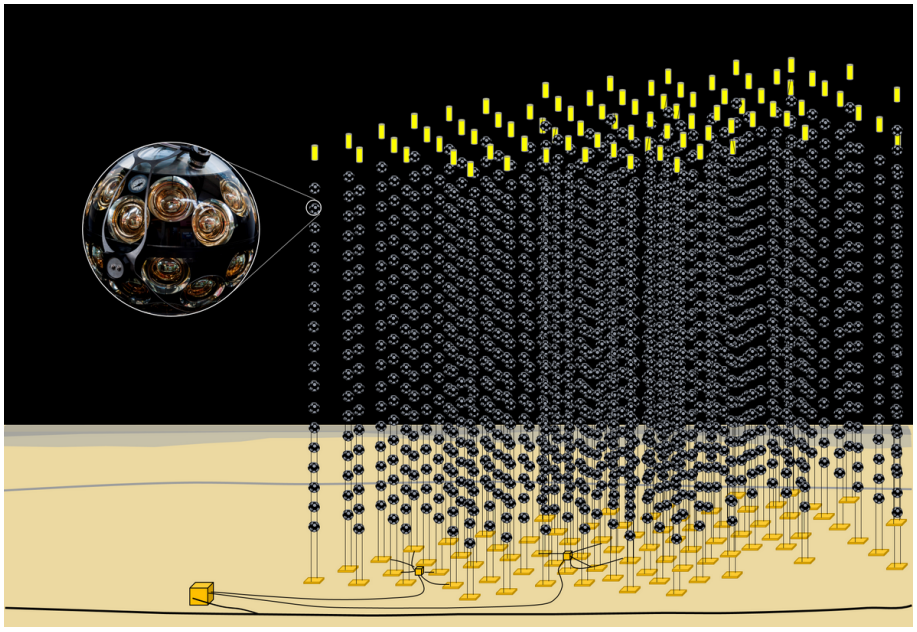

Figure 2: Schematic of a complete detection array with multiple detection strings connected to junction boxes, connected to the main data transmission line across the seabed.

The acoustic sensor inside the DOM is a piezo ceramic element as described in section 2.1. Furthermore, there are calibration units, whose bases host additional acoustic beacons, as well as hydrophones at known distances, that allow constant measurements of sound speed, which varies, depending on pressure, temperature and salinity of the water [14] [13].
The Time of Flight (ToF) between signal emission and reception is measured to determine distances between beacons and DOMs. With signals from at least three beacons, the DOM's position is calculated using multilateration, where each ToF measurement defines a sphere centered on the beacon, and the intersection of spheres determines the DOM location [13]. The data evaluation happens at the PC farms on shore. With consideration of more beacons and calibration data, the positioning accuracy is refined further. In addition, onboard tilt-meters (and compasses) within the DOMs provide orientation data, which aids in determining the local geometry of the detection units further increasing the localization accuracy.
While this system meets the desired accuracy, it is based on the assumption that the positioning signals (pings) propagate like plane waves in water, which introduces systematic uncertainties in the positioning system. These uncertainties can reduce angular resolution and might introduce errors in source identification. The assumption of plane waves is not the issue, as the beacons are far away relative to the diameter of the DOM. The problem arises, when the acoustic wavefront impacts the DOM away from the piezo sensor, as part of the energy couples into the glass shell and propagates through it as Lamb-like waves. Since the speed of sound in glass ($v_g \sim 5000\text{m/s}$) (see appendix C) is significantly higher than in seawater ($v_w \sim 1500\text{m/s}$) [8], these internal glass waves can lead to early arrival times that deviate from the assumed pure-water propagation model, as illustrated in figure 3.

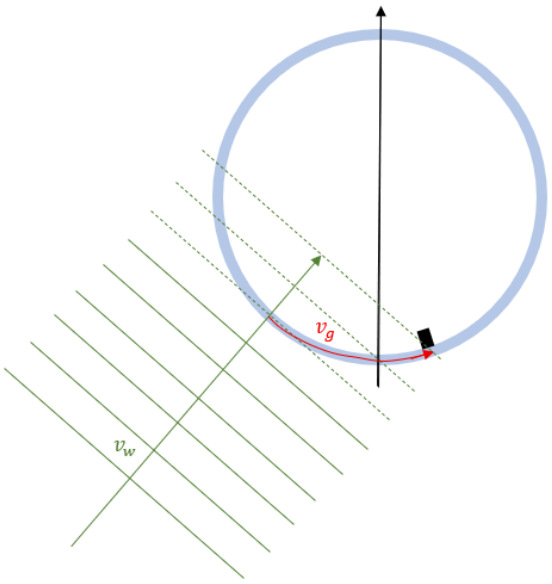

Figure 3: Illustration of the cross section of a DOM, with the black arrow representing its usual orientation. The black rectangle represents the piezo sensor. Planar wave fronts of the signal are represented by the green lines with propagation in the direction of the green arrow. Where the planar waves come into contact with the DOM an additional wave, propagating only in the glass is formed. The "glass-wave" reaches the piezo sensor before the plane wave, due to higher velocity.

Though this effect was studied for ANTARES using the modified AMADEUS system [6], a systematic analysis tailored to KM3NeT's signal shapes has not yet been performed. This thesis addresses that gap through finite element simulations of acoustic wave propagation in KM3NeT DOMs, in order to better understand and minimize these systematic errors. FEM is ideally suited for this task, as it can handle complex geometries, such as the DOM and account for material interfaces.
The procedure for this research is as follows. First the feasibility of simulations on this topic is researched, by comparing simulation results of simple geometries (thin plate) to theoretical expectation, in this case the formation of different lamb wave modes and dispersion. Next, the simulation of acoustic signals through a DOM is run with the goal of reproducing AMADEUS results, which adds a layer of validation, before the KM3NeT-signal is implemented and the newly obtained insight on Lamb wave propagation speed is discussed.

3 Lamb waves

Lamb waves are solutions to the partial differential equation governing an elastic system at its boundary. They describe energy propagating at the boundary of solid, elastic media as waves. More specifically, Lamb waves are the solutions to the problem of a solid isotropic plate with finite thickness and infinite lateral extent, commonly referred to as the *free plate problem* [15]. In solids, such as the plate, elastic waves either propagate through the bulk of the material or at the boundaries, called *bulk waves* and *guided waves* respectively. This differentiation makes Lamb waves a type of *guided waves*, meaning that they describe the displacement at the plate's boundary. They are the result of the interaction of elastic waves with the boundary by a way of reflection and refraction [15], more specifically the reflections between the top and bottom surface of a solid plate. The analytical solution to the equation of motion is difficult to obtain, as it is solved with respect to the boundary conditions, which is not the case for the bulk waves. In the following the free plate problem will be discussed, before the interesting insights are summarized for the simulation.

3.1 The free plate problem

The free plate problem describes a solid plate made from an isotropic material with finite thickness $d = 2h$ and an infinitely large base area, meaning the plate extends infinitely in the x_1 and x_2 Cartesian directions, as illustrated in figure 4. The infinite extension simplifies the calculations for the solution of the guided waves at the surfaces of the plate, as wave reflections and other interactions at the edges need not to be considered [16]. Furthermore, it is assumed that wave propagation is invariant along the x_2 direction, so that the displacement in the x_2 direction is zero for all times and all fields are only dependent on x_1 and x_3. This reduces the three-dimensional problem to a problem in the x_1-x_3-plane [16]. The result will still be sufficiently accurate, as the modes of displacement in the propagation direction (x_1) and the transverse, out-of-plane displacement (x_3) are of most interest. The shear modes in the x_2 direction exist independently of the other two modes and can be calculated with other methods [15]. This approach is known as the *plane strain assumption* and is a conventional method of solving the free plate problem [15]. It is consistent with classic treatments by Achenbach (1984) and Auld (1990) [15].

The differential equation governing the elastodynamic problem, can be deduced to the expression,

$$\mu u_{i,jj} + (\lambda + \mu) u_{j,ji} + \rho f_i = \rho \ddot{u} \tag{1}$$

where the term $\mu u_{i,jj}$ represents how shear deformation contributes to internal forces, with μ being the shear modulus (or second Lamé parameter) and $u_{i,jj}$ the second spatial derivative of the displacement with respect to x_j, or the Laplacian of the displacement in index notation. The expression $(\lambda + \mu) u_{j,ji}$ contributes to the internal forces due to volume changes, such as compression or expansion, in other words it describes longitudinal stress. Here λ is the first Lamé parameter, not the wavelength, which together with the shear modulus μ describes the material response. $u_{j,ji}$ represents the divergence of the displacement gradient in index notation. The final term of the left hand side describes external forces, where ρ is the material density and f_i is the ith component of the body force vector in units of force per mass [16].

Figure 4: Geometry of the free plate problem [15]. Only the x_1-x_3-plane is of interest.

The right hand side of the equation represents the inertial force per unit volume, with the structural acceleration ($\ddot{u}$) times the mass density ρ of the material.
To solve the equation the displacement field is rewritten according to Helmholtz decomposition

$$u = \nabla\phi + \nabla \times \psi \tag{2}$$

and substituted into (1). This results in two uncoupled wave equations, governing longitudinal and shear waves [15],

$$\frac{\partial^2\phi}{\partial x_1^2} + \frac{\partial^2\phi}{\partial x_3^2} = \frac{1}{c_L^2}\frac{\partial^2\phi}{\partial t^2}, \text{ for longitudinal waves;} \tag{3}$$

$$\frac{\partial^2\psi}{\partial x_1^2} + \frac{\partial^2\psi}{\partial x_3^2} = \frac{1}{c_T^2}\frac{\partial^2\psi}{\partial t^2}, \text{ for shear waves.} \tag{4}$$

with ϕ and ψ describe the displacement field of longitudinal and shear modes respectively. The equations describe the relation of the second spatial derivatives of the displacement fields to the second derivative in time, scaled by the respective mode speeds c_L and c_T. They describe how elastic disturbances propagate through the plate at characteristic speeds. In this calculation the speeds are defined as

$$c_L = \sqrt{\frac{\lambda + 2\mu}{\rho}} \text{ and } c_T = \sqrt{\frac{\mu}{\rho}} \tag{5}$$

The resulting displacements and stresses can be written in dependence of these new separate displacement fields [15].

$$u_1 = \frac{\partial\phi}{\partial x_1} + \frac{\partial\psi}{\partial x_3} \tag{6}$$

$$u_2 = 0 \tag{7}$$

$$u_3 = \frac{\partial \phi}{\partial x_3} + \frac{\partial \psi}{\partial x_1} \tag{8}$$

$$\sigma_{31} = \mu(\frac{\partial u_1}{\partial x_3} + \frac{\partial u_3}{\partial x_1}) \tag{9}$$

$$\sigma_{33} = \lambda(\frac{\partial u_3}{\partial x_3} + \frac{\partial u_1}{\partial x_1}) + 2\mu\frac{\partial u_3}{\partial x_3} \tag{10}$$

with the u_2 displacement being 0 according to the plain strain assumption and σ_{31} and σ_{33} the relevant components of the stress tensor. The solution is found by assuming infinite plane harmonic waves of the form [15]

$$\phi = \Phi(x_3)\exp(i(kx_1 - \omega t)) \tag{11}$$

$$\psi = \Psi(x_3)\exp(i(kx_1 - \omega t)) \tag{12}$$

these waves assume a harmonic plane wave solution in the x_1 direction ($\exp(i(kx_1 - \omega t))$), with an additional unspecified transverse wave shape $\Phi(x_3)$ or $\Psi(x_3)$ across the thickness of the plate. These assumed waves can be plugged into the governing equations for the different modes (3) and (4), to obtain classic second order differential equations of the form,

$$\Phi''(x_3) + p^2\Phi(x_3) = 0 \tag{13}$$

$$\Psi''(x_3) + q^2\Psi(x_3) = 0 \tag{14}$$

with $p^2 = \frac{\omega^2}{c_L^2} - k^2$ and $q^2 = \frac{\omega^2}{c_T^2} - k^2$.
These equations are solved with sinusoidal solutions,

$$\Phi(x_3) = A_1\sin(px_3) + A_2\cos(px_3); \tag{15}$$

$$\Psi(x_3) = B_1\sin(qx_3) + B_2\cos(qx_3); \tag{16}$$

which gives us the amplitude factor dependent on x_3 for the assumed harmonic waves (11) and (12). The displacements and stresses can be obtained by substituting the assumed waves into equations 6 - 10.

In a plate, two different modes need to be differentiated. For the symmetric mode, the u_3 displacement is symmetric with respect to the midplane of the plate ($x_3 = 0$), meaning that for a fixed x_1 the particles inside the plate either move away from the midplane or to the midplane equally, akin to a "breathing motion". Importantly this makes the u_1 displacement antisymmetric with respect to the midplane.
The antisymmetric mode describes the movement of all particles inside the plate to be an oscillation in the x_3 direction, meaning they all equally move "up" and "down" in the x_3 direction, resembling a "seesaw" motion. This implies, that the u_3 displacement is antisymmetric and the u_1 displacement symmetric, with respect to the midplane.
With the assumption of the two different modes we obtain two different sets of solutions, where the u_3 displacement is either only composed of sinusoidal terms (symmetric) or cosinusoidal expressions (antisymmetric). These solutions are the two fundamental types of *Lamb waves*, which are guided waves across a plates surface. The solutions for the symmetric and antisymmetric modes can be derived by substituting (11) and (12) into

the relations (6) - (10). For the different modes the respective amplitude factors $\Psi(x_3)$ and $\Phi(x_3)$ are

$$\Phi_{Sym} = A_2 \cos(px_3);\ \Psi_{Sym} = B_1 \sin(qx_3) \tag{17}$$

and

$$\Phi_{Asym} = A_1 \sin(px_3);\ \Psi_{Asym} = B_2 \cos(qx_3). \tag{18}$$

We have now successfully derived expressions for the different displacements, as well as the different stress tensor components for both possible modes of the free plate problem, with unknown amplitude parameters A_1, A_2, B_1, B_2 as well as no defined dispersion relation. These can also be determined by accounting for the boundary conditions. As we have a traction free boundary, the normal and tangential component of the strain vector need to vanish at the surface, so [15]

$$\sigma_{31} = \sigma_{33} \equiv 0 \text{ at } \ x_3 = \pm h. \tag{19}$$

For the symmetric modes application of these boundary conditions results in a homogeneous system of two equations with the parameters A_2 and B_1. Similarly, application to the solutions of the antisymmetric modes will give a homogeneous system of two equations with the parameters A_1 and B_2. The dispersion relation is obtained by requiring the determinant of the coefficient matrix to vanish, ensuring a non-trivial solution for the amplitudes. Under this condition we obtain an equation of the form

$$\frac{(k^2 - q^2)\sin(qh)}{2ikp\sin(ph)} = \frac{-2\mu ikq\cos(qh)}{(\lambda k^2 + 2\mu p^2)(k^2 - q^2)} \tag{20}$$

where p, q, λ and μ are defined as before, h is half the plates thickness and k the wave number. By utilizing the definitions of p and q, as well as the expressions $\lambda = c_L^2\rho - 2\mu$ and $c_T^2 = \mu/\rho$, derived from (5), this expression can be simplified.

$$\frac{\tan(qh)}{\tan(ph)} = -\frac{4k^2pq}{(q^2 - k^2)^2} \tag{21}$$

A more thorough calculation is done in [15]. With this equation we have a relation of the angular frequency ω and the wave number k for the symmetric modes. Equations of this nature are called *dispersion relations*. For a given ω, k can be derived and the displacements calculated with the equations derived before. Analogously a similar relation is derived for anti symmetric modes.

$$\frac{\tan(qh)}{\tan(ph)} = -\frac{(q^2 - k^2)^2}{4k^2pq} \tag{22}$$

Both of these relations are transcendental, which makes them unsolvable analytically and results are only obtainable by numerical methods. With these solutions the different Lamb mode propagation speeds can be calculated for different frequencies and plate thicknesses. In the calculation the material is assumed to be isotropic, which is not the case for most real materials, such as glass. A calculation for anisotropic materials is also possible, but would result in more complicated coupled equations. The fundamental approach however, is similar to the conducted calculation.

3.2 Application of the free plate problem

For the analysis of wave propagation in the finite plate, as well as the DOM shell the wave propagation cannot be calculated analytically. Instead it requires numerical methods such as the method of finite elements, discussed in section 4, to approximate the displacements. The discussion of the analytical free plate solution is important for understanding the formation of different propagation modes. An important remark regarding the rest of the thesis is, that *Lamb waves* are the solution to the ideal free plate problem, but that the simulation results of the finite plate model, as well as the glass spherical shell technically exhibit propagation of *Lamb-like waves*, meaning they behave similarly to theoretical Lamb waves.
In the following work these Lamb-like waves are often referred to as Lamb waves, for the sake of simplicity. The observation of Lamb-like waves in the simulated models is not surprising, as the finite plate behaves almost like the free plate for short time periods, before the propagating wave can interact with the sidewards boundaries. Furthermore, if the plate is large in comparison to the analyzed wavelengths, the Lamb like waves are expected to behave almost as derived analytically. In the plate geometry used later, with a base area of $63\,\mathrm{cm} \times 114.5\,\mathrm{cm}$ the expected wavelengths are

$$\lambda_{S_0} = \frac{v_{S_0}}{50\,\mathrm{kHz}} = \frac{5600\,\mathrm{m/s}}{50\,\mathrm{kHz}} \approx 11.2\,\mathrm{cm} \tag{23}$$

$$\lambda_{A_0} = \frac{v_{A_0}}{50\,\mathrm{kHz}} = \frac{3430\,\mathrm{m/s}}{50\,\mathrm{kHz}} \approx 6.86\,\mathrm{cm} \tag{24}$$

where S_0 is the symmetric base mode, A_0 the anti symmetric base mode. The expected speeds and the 50 kHz frequency are explained in detail in section 5. These wavelengths are sufficiently small for the free plate approximation to yield an accurate model of the finite plate's response over short time periods. With this in mind, the measurements of dispersion for the plate model are expected to follow the dispersion curves for Lamb waves, as calculated above.
Similarly, a spherical shell behaves like a curved plate, which is why Lamb-like waves are observed. In this geometry the free plate solution is not an accurate depiction of the problem, as boundary conditions and exact mode shapes are different for curved surfaces. However, the explanation for the formation of two different propagation modes is similar to the explanation earlier. There is different ways to approximate the wave propagation in spherical shells mathematically, which is not too relevant for this thesis as simulation results are compared to experimental data obtained from the modified AMADEUS experiment.

4 Finite Element Method (FEM)

This section outlines the basic principle of the finite element method, while omitting advanced mathematical details exceeding the scope of this thesis. It is useful to briefly introduce the FEM and why it is of interest for this project. In physics, the behavior of most systems and processes can be described mathematically, using partial differential equations (PDEs). These PDEs can quickly become quite complicated, which is why they are usually not analytically solvable for non idealized problems.
With discretization, numerically solvable equations can be constructed as approximations of the original PDE. From here an approximate solution for the problem can be determined via numerical methods. The FEM is a possible method to compute such approximations [1]. How exactly this computation works via FEM is best explained, when we consider the different steps separately. For simplicity, we can divide an approximation with FEM into three main steps. The discretization of the domain, the definition of material properties and boundary conditions and with it the construction of the system of equations and, lastly, the solving of these equations.

4.1 Governing equations

For the purposes of this thesis, the specific case of acoustic analysis is of greatest interest. The governing equations are the equations that determine the system response for given boundary conditions. In our case, the approximation of elastic wave propagation through solid material, the governing equations are

$$\rho \frac{\partial v}{\partial t} - \nabla \cdot S \;=\; F_v \tag{25}$$

$$\frac{\partial E}{\partial t} - \frac{1}{2}[\nabla v - (\nabla v)^T] \;=\; 0 \tag{26}$$

$$S \;=\; C : E \tag{27}$$

where v is the structural velocity, ρ is the density of the material, S is the stress tensor, E is the strain tensor, C is the elasticity tensor and F_v is a possible force vector [3]. Note that the : operator is a representation of a double contraction, as C is a fourth-order tensor. In the FEM formulation presented here, the elasticity tensor C is treated in general form, but unless specified otherwise, the simulations in this thesis assume isotropic elasticity. These equations describe the fundamental physics of an elasticity problem. As they are impossible to solve analytically for complex geometries, such as a KM3NeT module, we need to approach the calculation with FEM.

4.2 Discretization

Discretization is a critical step to construct a system of solvable equations. How it works is best explained with a simplistic example. Consider some one-dimensional function $u(x)$, which represents the primary field variable (e.g. displacement or structural velocity) of the physical problem. This function can be approximated with a finite amount of linear combinations of some basis functions Ψ_i from a suitable function space.

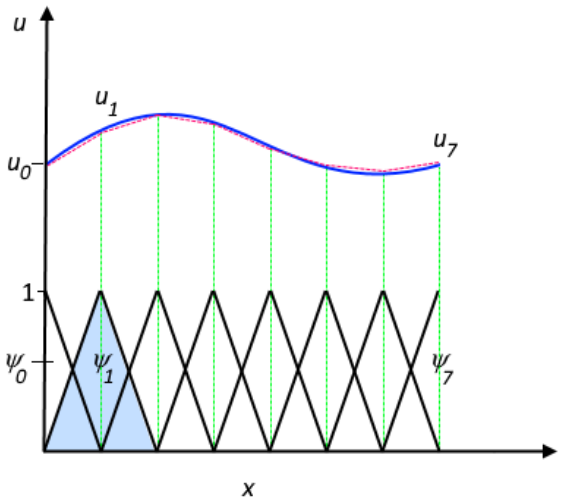

Figure 5: Visualization of the basic discretization principle. The blue line represents the original function $u(x)$, while the red, dotted line is the approximated function u_h. The solid black line represents the, in this case linear, basis functions, with which the linear combination is constructed. In this example we have 8 coefficients denoted u_0 through u_7. [1]

Mathematically this corresponds to,

$$u \approx u_h$$

with,

$$u_h = \sum_i u_i \Psi_i$$

where u_h is the approximated value of the function and u_i are the coefficients of the linear combination. To visualize this principle we consider 5 [2].

This discretization method works analogously for higher dimensions, as well as for a non-uniform distribution of elements unlike seen in figure 5. This means, that in locations, where a smaller approximation error is advantageous, such as system boundaries, the elements may be placed closer together.

4.3 The weak formulation

The calculation of the weak formulation of the PDE is a standard procedure in FEM. This is because it is a numerically solvable. Most importantly it still is based on the information of the original PDE, but is formed by projecting it onto a finite function space H [1]. This projection is often done with the Galerkin method. Technically it states that the solution parameters are defined by the equations

$$\int \Psi_j \, g \, dD = 0; \; j = 1, \; 2, ..., \; n \tag{28}$$

where D is the solution domain, Ψ_j are the test functions, and g is the residual of the PDE [2]. In the specific case of our momentum equation 29 we can calculate it [2]

$$\rho \frac{\partial v}{\partial t} - \nabla \cdot S \; = \; F_v \tag{29}$$

$$\rho \frac{\partial v}{\partial t} - \nabla \cdot S - F_v \; =: \; g(x,t) \tag{30}$$

Substituting the residual into the Galerkin condition 28 and applying the previously defined discretization to estimate the velocity field $v(x,t)$ yields

$$v(x,t) \; \approx \; v_h(x,t) \; = \; \sum_i v_i(t) \Psi_i(x) \tag{31}$$

to finally obtain [4]

$$\int \Psi_j \, (\rho \sum_i \frac{\partial v_i(t)}{\partial t} \Psi_i(x) - \nabla \cdot S(v_h) - F_v) \, dx \; = \; 0; \tag{32}$$

Important is, that in this formulation the boundary condition $\int \Psi_i \cdot (S \cdot n)$ (n is the surface normal) allows for any traction $(S \cdot n)$ at the boundary ∂D. [1] [4]. This equation produces large systems of equations that can be solved using linear algebra.

4.4 Solution

Finally we obtain a linear algebra problem of the form

$$M \frac{\partial v(t)}{\partial t} + Kv(t) = F(t) \tag{33}$$

In literature M is the so-called mass matrix which contains contributions from time-dependent terms (not to be confused with the elasticity tensor), K the stiffness matrix, which arises from spatial derivatives and material properties via the elasticity tensor C and F is a force vector [5]. Once assembled, the resulting system of ODEs is solved numerically using time-stepping schemes (e.g., implicit Euler), with FEM software like COMSOL automating much of the process. The following simulations all rely on these mathematical principles, although COMSOL automates most steps because of an intuitive user interface.

4.5 Sources of error in FEM

Finite element simulations are based on approximations, which introduces various sources of errors. In FEM the primary source of is the discretization of the domain, with errors depending on element size, particularly in regions, where the solution exhibits strong gradients. Additional inaccuracies may arise from the choice of the basis functions, numerical integration and the approximation of boundary conditions.
In sources like [4] and [2] the error sources are not always summarized explicitly although they identify discretization, modeling assumptions and numerical approaches as key factors influencing the error. Both sources provide great error estimation approaches, and cover different methods of minimizing the errors, including mesh refinement and appropriate time integration.
A detailed FEM error discussion lies beyond the scope of this thesis, but an awareness of these limitations is essential for critical analysis of the simulated resuls.

5 Simulations

The central focus of this work is the setup and analysis of simulations. As previously described, they are set up with the COMSOL multiphysics software. COMSOL allows for efficient geometry construction, selection of materials with different physical properties and setup of the necessary physics for numerical analysis.
For the most part the *elastic waves, time explicit (elte)* module in COMSOL was used. Alternative attempts were made with the *solid mechanics* module. Both modules solve the problem as described in section 4, although the *elte* module produced better results for time-explicit problems. Multiple complete setups were made, with results varying depending on different factors, such as mesh size, time-stepping and boundary conditions. This chapter focuses on the setups that yielded the most accurate results. In appendix A an overview of the simulation development process is presented.
Two geometries were analyzed to study elastic wave propagation. The first goal was to observe the propagation of *Lamb waves* in a thin glass plate and to compare the observed propagation speeds of the different modes with expected dispersion. Once the simulated results matched with expectation, the gained knowledge is applied to the more complicated geometry of the glass shell of a DOM. Once validated with AMADEUS experimental results, the final simulation was repeated with KM3NeT signal frequencies, which is the objective of this thesis.

5.1 Simulation 1: Glass plate

This subsection discusses the simulating process of the plate geometry. First, the simulation setup is briefly outlined, with more details provided in appendix B. Then, the results are analyzed and compared to theory.

5.1.1 Simulation setup

Geometry and materials The setup consist of two plates stacked atop of each other. Each has a rectangular base, with side lengths $d_y = 63$cm, which is the outer diameter of the OM glass and $d_x = 114.5$cm to analyze wave propagation across a larger distance. The plates each have different heights, $z_g = 15$mm for the bottom plate, which is the minimal thickness of the glass spherical shell and $z_p = 10$mm for the upper plate as shown in figure 6. On the top surface of the upper plate, a circular excitation area with a radius of $r_e = 40$mm is defined at the center. This area is subject to the boundary condition of an oscillating pressure, acting as the wave excitation. Because this problem is symmetric, it is cut in half, meaning the base of the plates are now 57.25 by 63cm as seen in figure 6. This reduces computational cost without sacrificing accuracy, as symmetry boundary conditions can be specified in COMSOL.
At the underside of the bottom plate there is 5 points, spaced 6cm apart, at which the displacement is tracked over time, as shown in figure 6.
The bottom plate is modeled with Vitrovex glass, while the top plate uses a plastic material with a density close to water. Material properties can be looked up in appendix C. The top plate was a later addition to this problem to simulate the waves going through water first, before arriving at the glass, which is an approximation of the real behavior of Antares or KM3NeT DOMs. While wave propagation in solids differs from that in liquids, this approximation is sufficient to produce representative results in the glass.

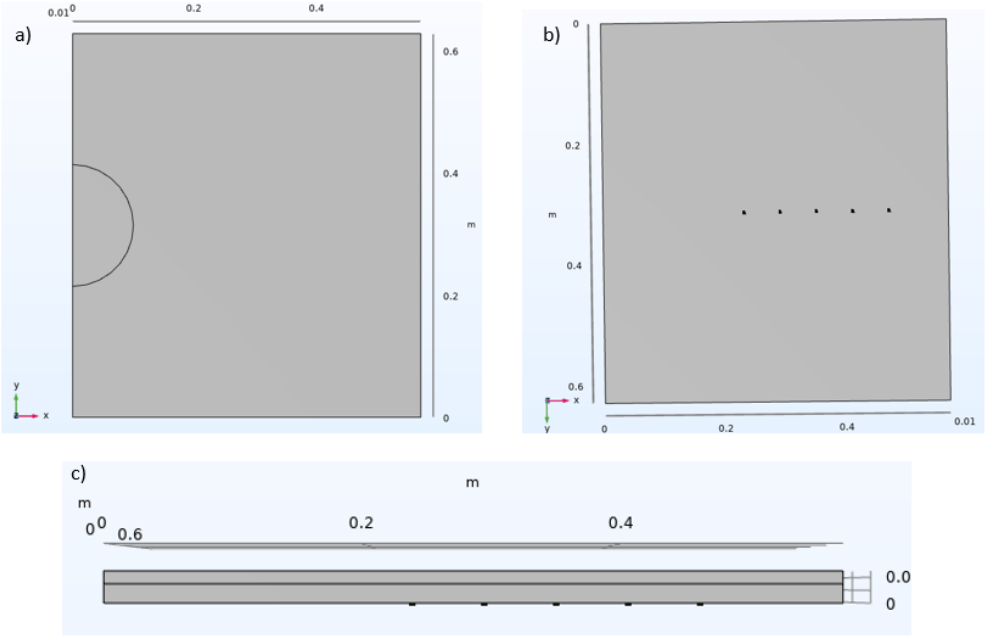

Figure 6: Simulated geometry as displayed in COMSOL. a) shows the top view, meaning the plastic plate points in our direction, b) is the bottom view with the glass plate visible and c) is the side view of the problem. We can see, that everything is cut in half because of symmetry. In a) the excitation area is visible. In b) we see the point probes.

Boundary conditions Next, the boundary conditions are defined. In this simulation, the sideward surfaces are set to be low-reflecting, to reduce interferences. The surfaces at the symmetry plane are defined to be symmetry boundaries. The upper and bottom side are set to be free boundaries as presented in figure 7. The spherical excitation area will be used to exert a boundary load, which is our pressure signal. In between the two plates we need to define how the program should handle the touching faces 7. This will be realized with an identity boundary pair, which makes the fields across the entire connecting side continuous [7].

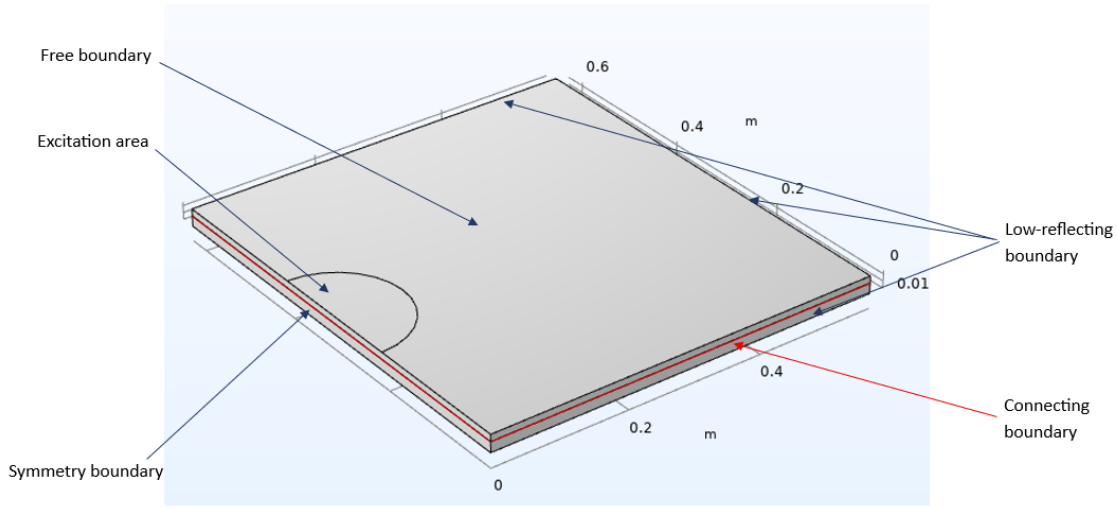

Figure 7: This figure specifies how the boundaries are defined. Note the the arrows pointing to the side faces mean, that top and bottom plate are defined with this condition. The connecting boundaries are the two touching surfaces in between the plates.

Excitation signal The excitation pressure is modeled after the ANTARES localization signal, also used in the AMADEUS experiment [6]. The time dependent signal is a cosine wave 34

$$S_0(t) = A \cdot \cos(2\pi f_0(t - t_d) \tag{34}$$

where A is the amplitude, f_0 is the signal frequency and t_d is a time delay. It is modulated with a Gaussian envelope with respect to time 35.

$$G_t(t) = \exp\left(-\frac{(t - t_d)^2}{2\sigma^2}\right) \tag{35}$$

where σ is the width of the Gaussian envelope. In addition, another modulation of the signal with two step-down functions, forming a signal window is multiplied 36.

$$W(t) = \left(1 - \frac{1}{\exp\left(\frac{t-t_0}{\lambda}\right) + 1}\right) \cdot \left(\frac{1}{\exp\left(\frac{t-t_1}{\lambda}\right) + 1}\right) \tag{36}$$

Here t_0 is the start time of the window, t_1 the end time and λ defines how sharp the step is. To reduce sharp cut-offs in the signal pressure at the edges of the excitation area, as in earlier simulation versions described in A, another Gaussian envelope is multiplied with respect to space 60.

$$G_r(x, y) = \exp\left(-\frac{(x - x_0)^2 + (y - y_0)^2}{r_0^2}\right) \tag{37}$$

with x_0 and y_0 being the coordinates of the circles center and r_0 the radius. This envelope ensures a smooth decay in pressure from the center of the excitation area.

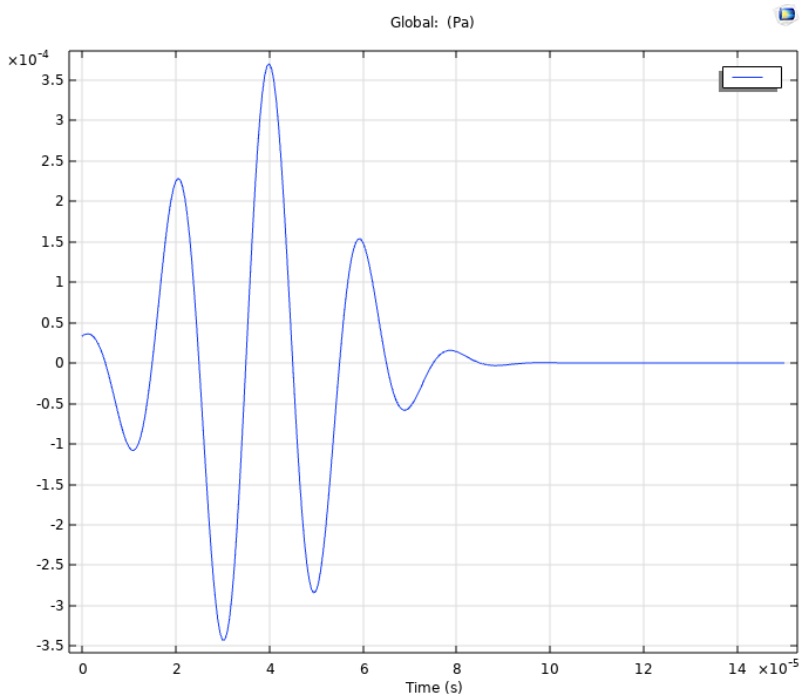

Figure 8: The resulting signal shape with respect to time. The spatial modulation is observed to be working as well.

The final signal applied at the boundary is:

$$S(t, x, y) = S_0(t) \cdot G_t(t) \cdot W(t) \cdot G_r(x, y) \tag{38}$$

With the parameters $A = 5\,\text{mPa}$, $f_0 = 50\,\text{kHz}$, $t_d = 50\,\mu\text{s}$, $\sigma = 20\,\mu\text{s}$, $t_0 = 10\,\text{ns}$, $t_0 = 60, \mu\text{s}$ and $\lambda = 15\,\mu\text{s}$ a nice signal form is accomplished, visualized in figure 8. The spatial gauss window is dependent on geometry definition and for this exact geometry is defined in the modeling instructions in appendix B. These parameters were adjusted by trial and error and ensure a well shaped signal, resembling the signal shape of the localization signals used in AMADEUS [6].

Meshing Meshing the geometry is a critical step, as it defines how many elements are created. With finer elements a more accurate result is achieved at the cost of more computation. As the observation of lamb waves propagating through the glass is of most interest, the expected wave speeds need to be considered. Two wave modes are expected as explained in section 3, with expected propagation speeds in Vitrovex glass [6]

$$v_{long} = \sqrt{M/\rho} = 5.60\text{mm}/\mu\text{s} \tag{39}$$

$$v_{trans} = \sqrt{G/\rho} = 3.43\text{mm}/\mu\text{s} \tag{40}$$

with $M = 70.00\,\text{GPa}$ the P-wave modulus and $G = 26.25\,\text{GPa}$ the shear modulus of the glass.

According to COMSOL documentation [7] the maximum element size h_{max} for studying elastic wave propagation is

$$\frac{c_{min}}{2 \cdot f_{max}} < h_{max} < \frac{c_{min}}{1.5 \cdot f_{max}} \tag{41}$$

This would mean that the maximum element size needs to be within a width of the element $34.3\,\text{mm} < h_{max} < 45.7\,\text{mm}$ for the given parameters. However, for accurate lamb wave simulations, this value is too coarse. Therefore, a maximum element size of $h_{max} = 16\text{mm}$ is used, which provides a suitable compromise between resolution and computational cost. After meshing the geometry, a time dependent study is set up. In total $150\,\mu\text{s}$ is simulated with the time steps each being $0.5\,\mu\text{s}$.

5.1.2 Simulation results

Several types of curves can be generated with this simulation. These include pressure, structural velocity and displacement curves, as well as 3D animations of velocity and pressure across the structure. For the purposes of this analysis, the displacement curves are of most relevance, as the piezo sensors utilized in AMADEUS also measure a voltage that is proportional to the displacement. Other types of curves, and the reasons, why they were not utilized are discussed in appendix A. Multiple displacement curves were generated, enabling an analysis of signal propagation speed. This is best conducted by plotting $u(t)$-curves at the points marked in figure 9, where u denotes the displacement at each point probe. Additionally, $u(x)$-plots were generated along the underside of the glass, which is a valuable benefit of simulations, as this plot would be hard to measure experimentally. For this, a cut-line 3D object is set up in the results tab, also shown in figure 9.

The wavefront reaches the cut line object at approximately $t_a = 60\mu\text{s}$. For wave speed analysis the $u(x)$-plots are best suited at times in between 100 and $140\mu\text{s}$. For these times the different lamb wave modes are clearly visible propagating across the plate. At earlier times the waves have not fully propagated and at later times, the results become less reliable due to interferences from reflections and potential numerical artifacts. The propagation speed is easily measured by plotting multiple $u(x)$-curves for different times as seen in figure 10 and measuring the distance between different maxima. The different times are always $t_s = 10\,\mu\text{s}$ apart, which simplifies the speed calculation.

With known values Δx_l ; Δx_t and $\Delta t = t_s = 10\mu\text{s}$ the propagation speed is calculated. The travel distance is measured for adjacent, corresponding peaks as shown in 10. These curves are not completely continuous, which is expected of a finite element simulation and their resolution mostly depends on utilized element size. For an accurate speed measurement, the local maxima are determined, and the corresponding x-values are utilized for speed computation. The mean of the calculated speed values is then formed to give an accurate result.

$$v_t = (2.18 \pm 0.06)\,\text{mm}/\mu\text{s} \tag{42}$$

$$v_l = (5.35 \pm 0.08)\,\text{mm}/\mu\text{s} \tag{43}$$

these values are significantly lower, than calculated before, due to dispersion effects described in section 3.

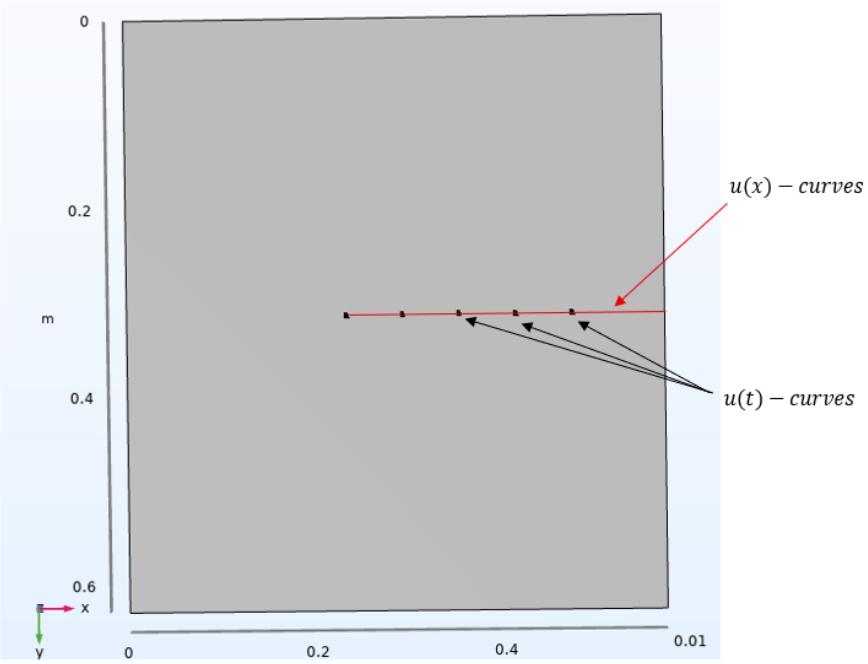

Figure 9: The picture shows the underside of the glass plate with the different black point probes and the red cut-line-3D-object.

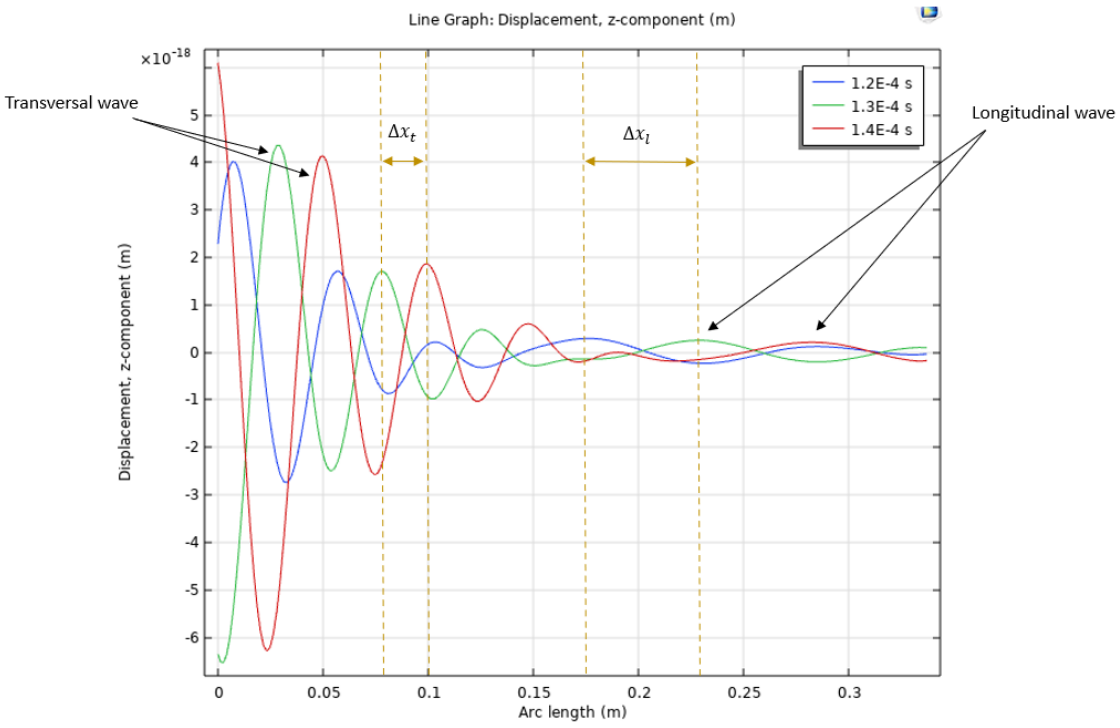

Figure 10: $u(x)$-plots for different time steps $t_s = 10\mu$s. The wave propagation of the different modes is clearly visible. The longitudinal mode has a much smaller amplitude and travels faster than the transverse mode.

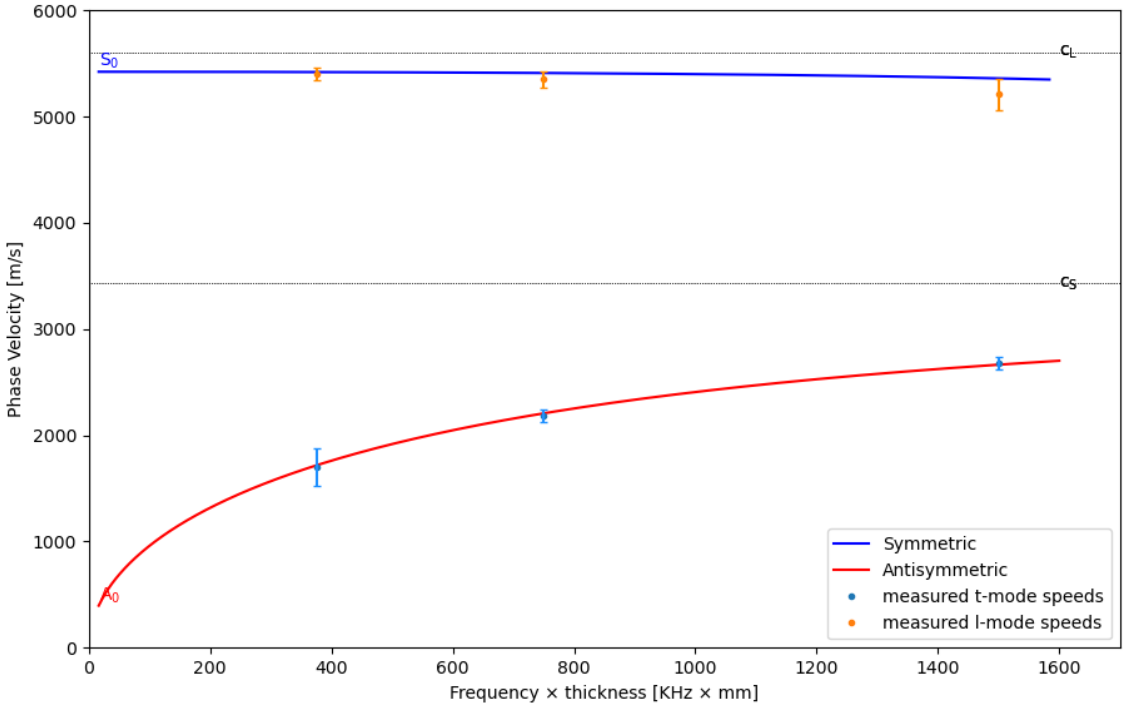

Figure 11: Phase velocity vs. frequency×thickness dispersion plot. The continuous lines represent the theoretical dispersion relation as derived in section 3. The dashed lines labeled c_L and c_S represent the calculated values v_{long} and v_{trans} respectively. The measured values and their errors are marked in orange and blue.

To further analyze dispersion, a similar simulation was conducted. This time the glass plate has a thickness of $z_g = 7.5\,mm$. According to the correlation of the $frequency \times thickness$ product and the wave propagation speeds, this should yield different propagation speeds. A third simulation was also performed with $z_g = 30$mm, providing three data points for a dispersion curve. The speeds are calculated as before with the curves as shown in figures 25 and 26 which are located in appendix D. The speeds from these additional simulations are:

$$v_{t,7.5mm} = (1.70 \pm 0.18)\,\mathrm{mm}/\mu\mathrm{s} \tag{44}$$

$$v_{l,7.5mm} = (5.40 \pm 0.06)\,\mathrm{mm}/\mu\mathrm{s} \tag{45}$$

and

$$v_{t,30mm} = (2.68 \pm 0.06)\,\mathrm{mm}/\mu\mathrm{s} \tag{46}$$

$$v_{l,30mm} = (5.21 \pm 0.15)\,\mathrm{mm}/\mu\mathrm{s} \tag{47}$$

These values will now be plotted, to confirm that expected dispersion is observed. Figure 11 shows a dispersion plot with the speed measurements for different plate thicknesses and the theoretical dispersion curve for Lamb waves, as calculated in section 3 for Vitrovex glass. The dispersion plot shows, that the measured values align with the theoretical curves, confirming that the observed wave propagation exhibits Lamb-like behavior.

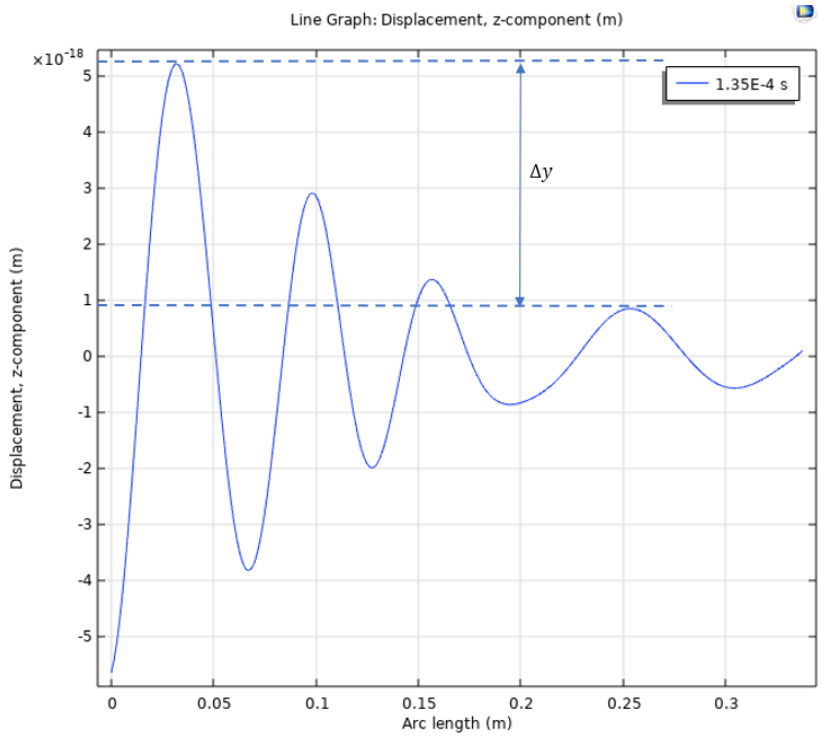

Figure 12: $u(x)$ of the 30 mm plot for a time, where the highest peak of the transverse wave is visible. The ratio is calculated with the highest peak value of the transverse wave and the highest peak value of the longitudinal wave.

Although the speeds are the main interest in this analysis another interesting observation is made regarding the amplitudes. In all measurements for different plate thicknesses, the longitudinal wave has a much lower amplitude, than the transverse wave. If however, the ratio of those two amplitudes is considered, it is observed, that with increasing wave thickness, this ratio increases. This ratio is defined as

$$R = A_{\text{trans}}/A_{\text{long}} \tag{48}$$

with the amplitude values A_{trans} and A_{long} as illustrated in figure 12. the ratios for the different plate thicknesses are calculated utilizing the plots 28 and 27, found in appendix D and the one seen in 12. The calculated ratios are,

$$R_{7.5\text{mm}} = 0.012 \tag{49}$$

$$R_{15\text{mm}} = 0.034 \tag{50}$$

$$R_{30\text{mm}} = 0.163 \tag{51}$$

This demonstrates, that the amplitude ratio of transverse and longitudinal wave also depends on plate thickness. The cause of this trend, will not be further discussed in this thesis, but a comparison of these ratios to AMADEUS results is made in the context of the DOM geometry.

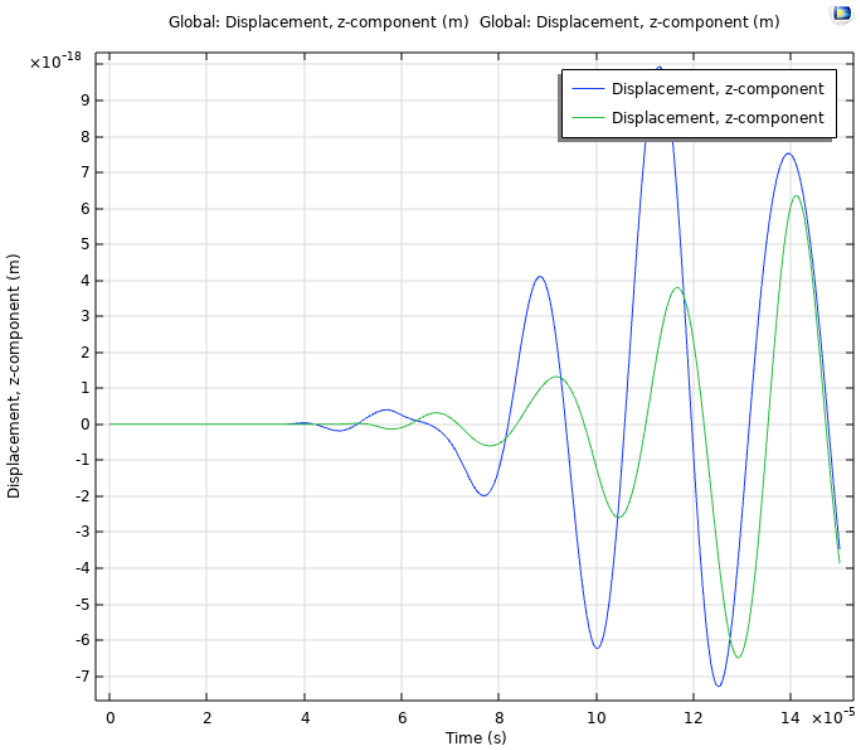

Figure 13: The $u(t)$-curves for the first two point probes at $x_1 = 175$mm and $x_2 = 235$mm. Both wave modes can be seen.

In addition to the $u(x)$ plots, the $u(t)$-plots shown in figure 13, also clearly illustrate the propagation of lamb waves. These plots are mainly interesting for comparison with the AMADEUS results, as the longitudinal wave is not as accurately distinguishable as in the $u(x)$-plot and they were not utilized for speed calculations. A comparison of these plots and the experimental AMADEUS plots is done for the $u(t)$ curves generated in the DOM-simulation, as the plate geometry introduces a major difference in analyzed geometry, which makes the plate results incomparable to the experiment.
An additional observation from figure 13, is how the simulation accounts for wave attenuation. In physical materials, signal amplitude decreases, due to the energy loss. This simulation replicates this behavior. In figure 13, the amplitude decreased over the traveled 60 mm. By measuring the amplitude of the highest peak in both probe plots, the amplitude decreased by 36 %. For probes farther from the source plotted in figure 29, found in appendix D, an amplitude decrease of 15 % over a traveled distance of 60 mm is measured. While a detailed comparison to theoretical attenuation is beyond the scope of this work, these results confirm that the simulation realistically models wave damping. Overall, the plate simulation provides a strong foundation for the spherical model. It confirms the expectation of lamb like wave propagation and allows for credible speed measurements. In the next subsection this spherical shell is simulated and the physically relevant propagation speeds extracted from the results.

5.2 Simulation 2: Glass spherical shell

In this subsection, the process of simulating the DOM geometry is briefly described, with exact modeling instructions found in appendix B. In the second part of this section the results are presented. Two separate simulations are conducted with different excitation signal frequencies. The first replicates conditions from the AMADEUS experiment, validating the methodology. The second uses lower frequencies replicating the KM3NeT positioning signal. Reproducing the AMADEUS results adds credibility to the extracted wave speeds at KM3NeT frequencies.

5.2.1 Simulation setup

Geometry and materials The geometry of this simulation is composed of two primary components. A spherical shell with an outer radius of $r_o = 216\,\text{mm}$ and an inner radius of $r_i = 201\,\text{mm}$. This makes the shell 15 mm thick, which is the minimal thickness specified for the shells used for the DOMs [11]. The inside of the shell is empty, meaning it is treated as a vacuum on the inside by the simulation. Furthermore, the shell is embedded at the center of a plastic cube with side lengths $l = 452\,\text{mm}$, mimicking the water around the DOM.
On the inner surface of the glass shell there is a total of seven points, placed in equal distances of each other across the upper quarter of the shell. These points will become the point probes, at which the $u(t)$ displacement curves are measured as shown in figure 14. To optimize computational efficiency, geometric symmetry is exploited by modeling only half of the system. A symmetry boundary condition is applied along the central plane, as in the previous plate simulation. The spherical shell is assigned the material properties of Vitrovex glass, while the surrounding cube is made of the same plastic material, as utilized in 5.1. An overwiew of the geometric properties and boundary conditions is presented in figure 14.

Boundary conditions As in the previous simulation, the boundaries need to be defined. All outward facing surfaces, except the top face, are set as low-reflecting boundaries to suppress artificial reflections that could affect the resulting curves. Furthermore, all faces at the cut plane are selected as symmetry boundaries. A boundary load is applied uniformly across the entire upper surface, to simulate plane waves arriving at the DOM. To ensure continuity between block and spherical shell, an identity boundary pair condition is utilized, making the fields across the touching faces of DOM and block continuous. The exact application of this condition is explained in the modeling instructions in appendix B. All remaining surfaces are set to be free boundaries. An overview of the applied boundary conditions is visualized in figure 14.

Excitation signal The pressure signal applied at the upper surface is similar to the signal utilized in the first simulation. It consists of the product of three different temporal functions, as defined in equations 34 through 36 fulfilling the already described purposes:

$$S(t, x, y) = S_0(t) \cdot G_t(t) \cdot W(t) \tag{52}$$

with $S_0(t)$ defined as in equation 34, $G_t(t)$ like in equation 35 and $W(t)$ from equation 36.

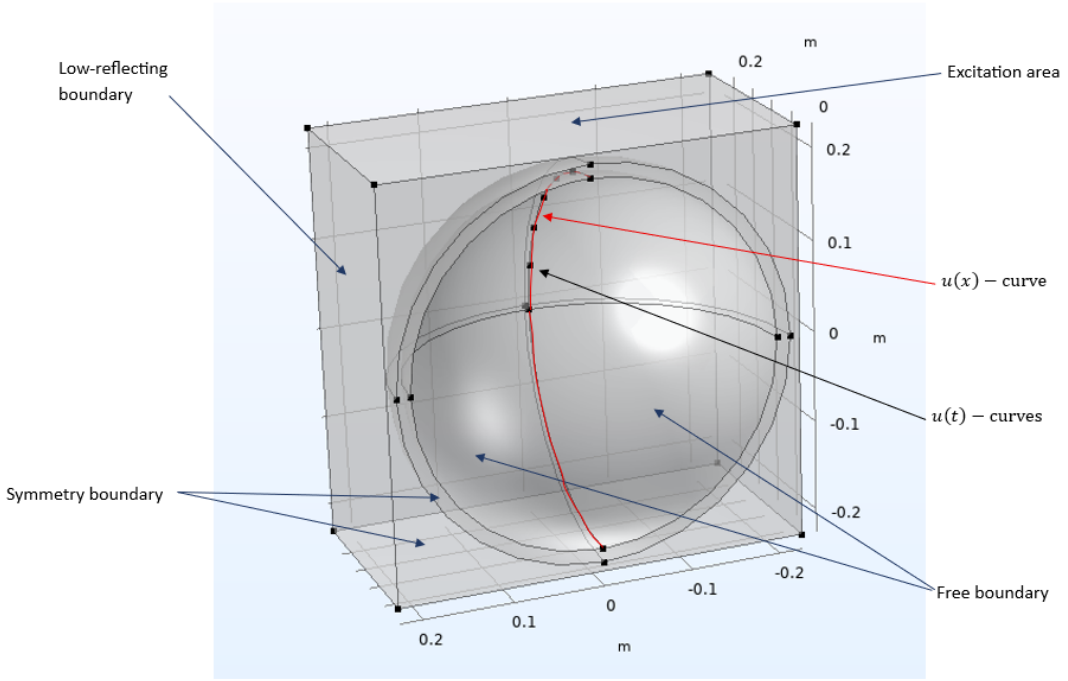

Figure 14: Utilized geometry as displayed in COMSOL. The geometry is cut in half making use of the symmetry to reduce computational cost. The boundary conditions for the different faces are described.

In this case the spatial gaussian is not applied, ensuring the pressure to be equal across the whole surface, mimicking a plane wave.
The parameters are chosen as before, so $A = 5\text{mPa}$, $f_0 = 50\text{kHz}$, $t_d = 50\mu\text{s}$, $\sigma = 2\mu\text{s}$, $t_0 = 10\text{ns}$, $t_0 = 60\mu\text{s}$ and $\lambda = 15\mu\text{s}$, producing a shape as seen in figure 8.
This signal replicates the signals utilized in the AMADEUS experiment, where frequencies of $f_0 = 50\,\text{kHz}$ where utilized. After simulating with the 50 kHz signal the simulation is repeated with a signal frequency of $f_0 = 20\,\text{kHz}$, aligning with KM3NeT's positioning signal frequency range 20 kHz to 40 kHz [13].

Meshing Meshing of this geometry has the same requirements as before, and needs to be optimized for the observed wavelengths. The mesh sizes utilized for the plate with a maximum element size of $h_{max} = 16\,\text{mm}$, this larger geometry allows for a slightly coarser mesh without compromising accuracy. Therefore, a maximum element size of $h_{max} = 18\,\text{mm}$ is used to reduce simulation runtime.

5.2.2 Simulation results

As before, the resulting displacement curves are analyzed, for the reasons discussed above. The $u(t)$ and $u(x)$ plots are measured along the inner side of the glass shell as seen in figure 14, because the piezo sensor is also located inside the DOM. Propagation speed is measured with the $u(x)$ curve with the same method utilized in the plate simulation.
First, the results of the simulation with a signal frequency of $f_0 = 50\,\text{kHz}$ are discussed and compared to the AMADEUS experiment results. Later, the propagation speeds are

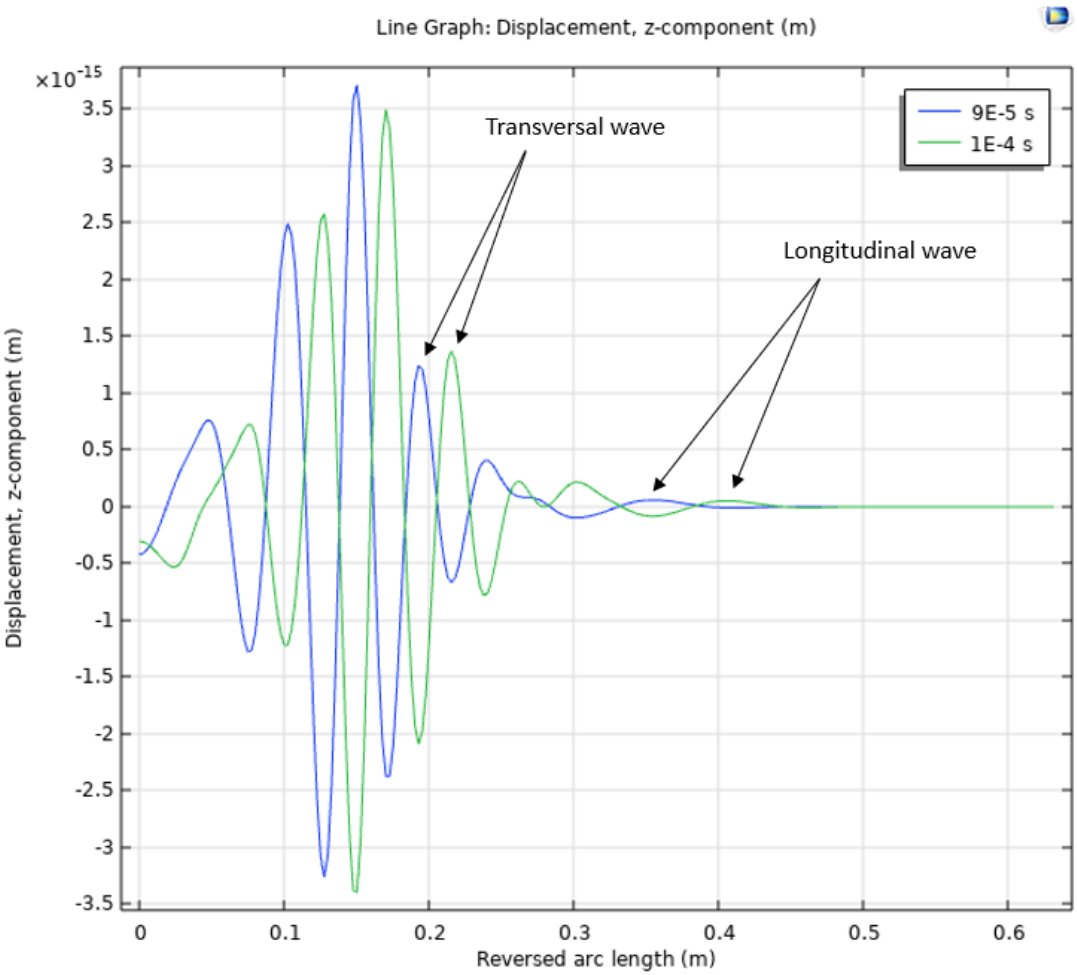

Figure 15: The plot shows the $u(x)$ z-displacement for the times $t_1 = 90\,\mu$s and $t_2 = 100\,\mu$s, across the red line marked in figure 14. The propagation of two modes, longitudinal and transverse, is observed.

calculated for the second simulation with a signal frequency of $f_0 = 20\,$kHz. With these speed values a potential correction for the positioning in KM3NeT can be derived.

50 kHz signal The $u(x)$-plots for the 50 kHz simulation are generated and analyzed first. With these plots the propagation speeds of the two observed modes are calculated analogically to the method displayed in figure 10. The utilized $u(x)$-plot is seen in figure 15.

In the plot both wave modes are clearly visible. Using three time steps for improved accuracy seen in figure 30,located in appendix D average propagation speeds are calculated as:

$$v_t = (2.21 \pm 0.14)\,\text{mm}/\mu\text{s} \tag{53}$$

$$v_l = (5.02 \pm 0.05)\,\text{mm}/\mu\text{s} \tag{54}$$

In the AMADEUS experiment the propagation speeds of both waves were measured

for a signal of frequency $f = 50\,\text{kHz}$. The simulated propagation speeds are compared to the the measured speeds in this experiment [6, Table 3]:

$$v_t = (2.04 \pm 0.01)\,\text{mm}/\mu\text{s} \tag{55}$$

$$v_l = (5.16 \pm 0.09)\,\text{mm}/\mu\text{s} \tag{56}$$

The simulated results closely match experimental results. The measured speed for the transverse (late) wave is slightly overestimated, while the speed for the longitudinal (early) wave slightly underestimated. If the errors are taken into account, the simulated speeds are a rather accurate representation of the experimental results, although the speeds of the late wave are not within the standard deviation errors. These discrepancies likely arise from discretization errors in identifying wave peaks, which could be minimized with finer meshing.
As was the case for the plate simulation, the amplitude of the early wave is consistently lower than the amplitude of the late wave. In AMADEUS the measured amplitude ratio was approximated to be roughly $\sim 1:10$ [6]. Using peak values from figure 15, the amplitude ratio is calculated for the simulated case, analogously to the ratios in the plate simulation as illustrated in figure 12. The measured ratio is roughly $\sim 2:100$, which is a lot lower than the estimate of the AMADEUS results. This can be explained because of the different method of measuring the ratio. In AMADEUS, the ratio is calculated with the second maxima of each wave. Re-calculating the ratio with this approach yields a ratio of $\sim 5:100$, demonstrating reasonable agreement and reinforcing the qualitative behavior of a weak, fast wave and a stronger, slower one.

The $u(t)$-plots are generated for the probe locations at the previously defined points with x and z-coordinates $x_1 = \cos(\pi/6) \cdot 201\,\text{mm}$, $z_1 = \sin(\pi/6) \cdot 201\,\text{mm}$ and $x_2 = \cos(\pi/12) \cdot 201\,\text{mm}$, $z_2 = \sin(\pi/12) \cdot 201\,\text{mm}$ respectively. To accurately compare the resulting curves with the AMADEUS experimental results, the distance to the the point of impact (POI), i.e. the point on the glass sphere, where the plane waves first interact with the material, need to be calculated. As the POI in the simulation is conveniently defined to be at coordinates $x_{POI} = 0$ and $z_{POI} = r_o$, with r_o the radius of the outer sphere of the shell, this calculation is easily done. For the sake of simplicity the distance is calculated relative to the POI of the inner sphere so with $z_{POI} = r_i = 201\,\text{mm}$, which should not have much of an impact on the results. The distance to the probes from the POI are exactly $\frac{5}{24}$ and $\frac{6}{24}$ of the whole inner circumference $c_i = 2\pi \cdot 201\,\text{mm}$. The distances from the POI to the first probe is $\frac{5}{24}c_i \approx 263.2\,\text{mm}$ and the distance in between the POI and the second probe is $\frac{6}{24}c_i \approx 315.7\,\text{mm}$. These values are important for the comparison made later. The recorded $u(t)$-plots are seen in figure 16.

In these plots there is a clear distinction between both waves visible. Using this plot for rough estimation yields similar speeds:

$$v_{t,u(t)} \approx 2.21\,\text{mm}/\mu\text{s} \tag{57}$$

$$v_{l,u(t)} \approx 5.20\,\text{mm}/\mu\text{s} \tag{58}$$

Wave attenuation is observed as reduced amplitude at the farther probe, although interference makes precise amplitude comparison difficult.

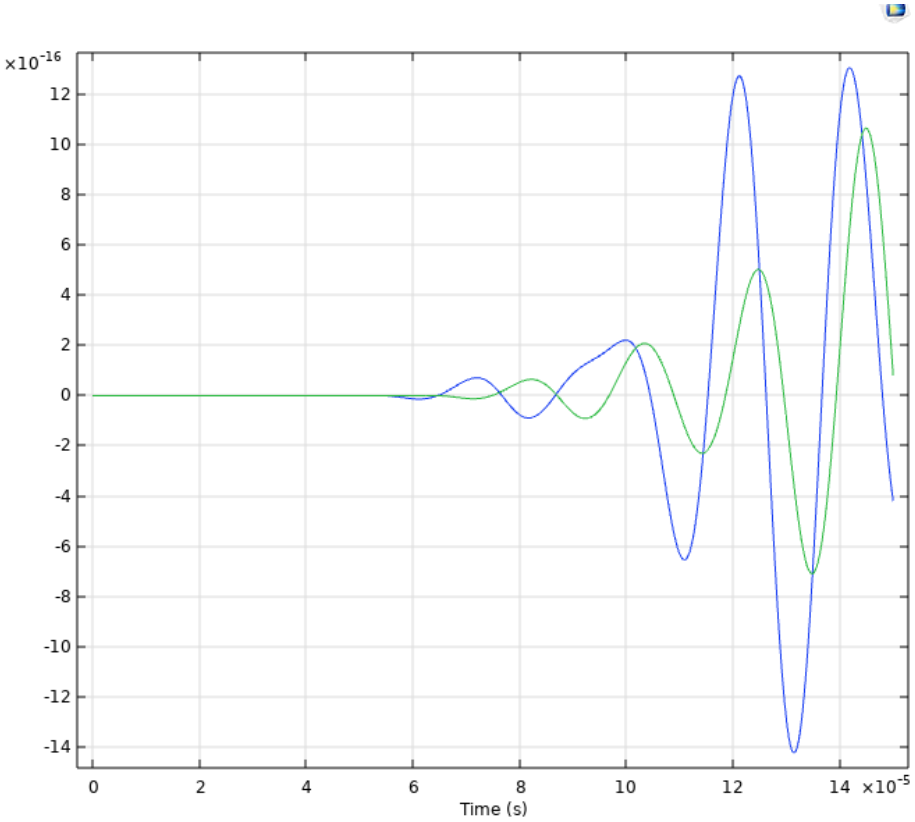

Figure 16: $u(t)$-plots for the two distances from the POI as described in the text. The blue curve is the displacement for the closer probe and the green curve is the displacement at the point farther from the POI. Here in both curves the first peak of the early wave is visible in both plots. The late wave with the original signal shape is clearly visible in both curves.

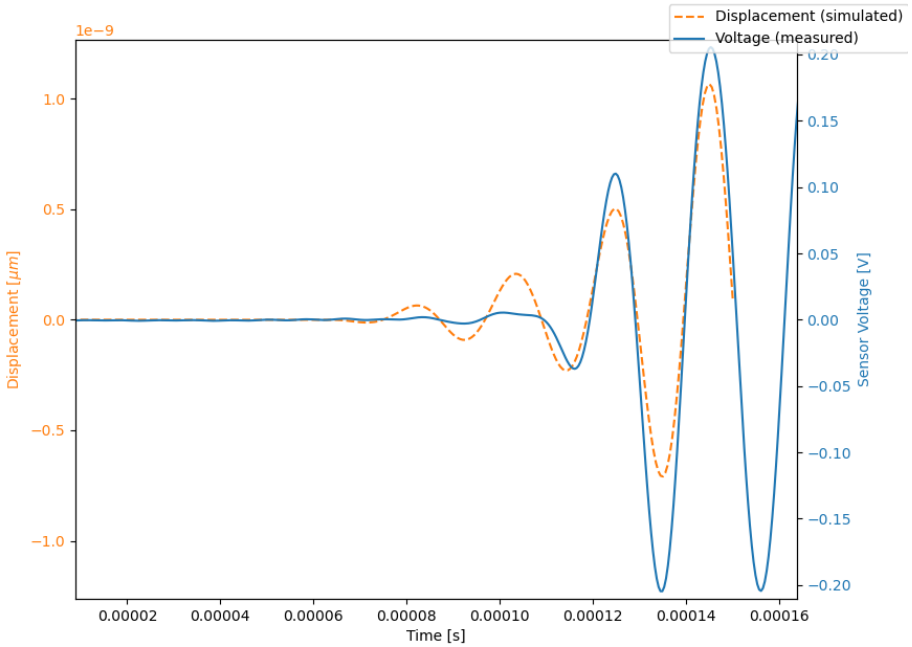

Figure 17: The piezo readings of the sensor located 300 mm away from the POI from the AMADEUS experiment are marked with the blue line. The simulated displacements for the probe 315 mm away from the POI. The amplitude of the early wave in the measurements are a lot smaller than in the simulation.

To compare the simulated $u(t)$ curve with AMADEUS measurements, the displacement curve at 315.7 mm is overlaid with piezo sensor data from AMADEUS at ~ 300 mm. The distances from the POI need to be similar for both measuring points, because the early wave will have separated from the late wave to similar amounts. The plot is generated using python with the data from AMADEUS for the 50 kHz signal for the correct sensor and the exported data from COMSOL for the correct probe. Both signals are scaled and aligned using the late wave peak. The x-axis is an arbitrary time axis. The plot is seen in figure 17.

In this figure the peaks for the late wave were aligned and the first observation is that the frequencies utilized are the same. An alignment of the early wave peaks is conceptually visible, although the amplitude of the measured values is quite low, which makes it difficult to properly identify the early wave. Furthermore, the distance of the sensor to the POI in the experiment is estimated to be accurate up to $\pm 10 - 15$ mm, limiting the precision of this comparison further. However, especially at the first early wave minimum of the blue curve an alignment of the early waves is visible, confirming that simulation and experiment observe similar wave behavior. In a more controlled environment, with better comparison standards, as well as a more sophisticated simulation setup, this comparison might be better possible.

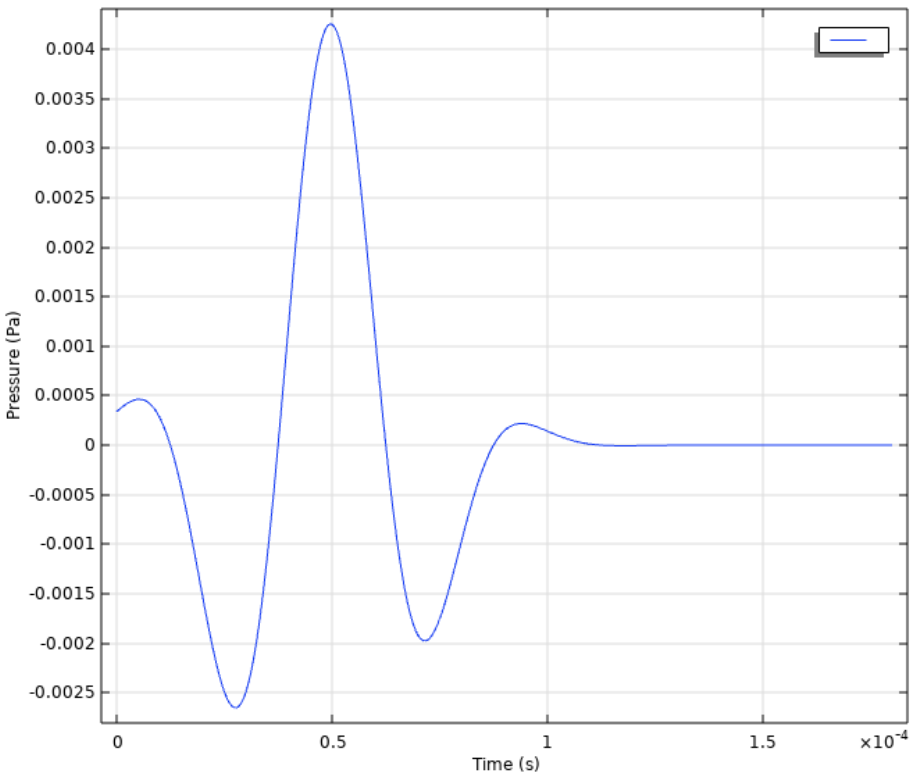

Figure 18: Signal shape of the 20 kHz signal utilized as the excitation of the plastic plane waves. In total it compromises less oscillations.

20 kHz signal As the measured speeds in the 50 kHz simulation were quite close to the ones measured in AMADEUS, the simulation is repeated with a KM3NeT 20 kHz positioning signal.
The signal has the same shape as described in equations 34 through 36, although the parameters were modified to accomodate the lower frequency.
The parameters modified is the time gaussian width $\sigma = 25\,\mu$s, the end time $t_1 = 80\,\mu$s and of course the frequency $f_0 = 20\,$kHz. This new signal is plotted in figure 18. Because of these changes in signal shape the simulation is extended to $180\,\mu$s and the meshing size increased, to an maximum element size of $h_{max} = 20\,$mm, to reduce computational cost.

A simulation over a longer time period, with an excitation signal compromised of more full oscillations like in figure 8, could produce better results, however, this was not attempted as the simulation would have significantly longer run times.
Figure 19 shows the $u(x)$ displacement at $t = 100\,\mu$s and $t = 110\,\mu$s, as this kind of plot proved to be effective for propagation speed calculation.

Both wave modes are visible, though the early wave shows a prominent and unexpected negative peak, which is likely a numerical artifact. The propagation of both modes is accurately observable and the speeds are measurable. In the $u(x)$-plot the waves clearly propagate slower then in the 50 kHz $u(x)$-plot 10 and the speeds are calculated as before.

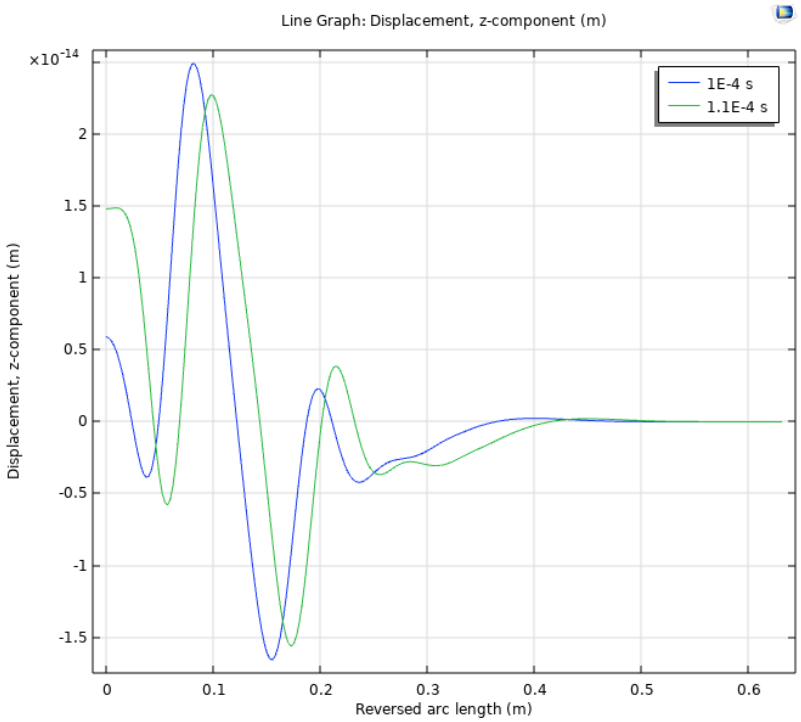

Figure 19: $u(x)$-plot for the times 100 μs and 110 μs. Both waves are visible, but the early wave has a lower amplitude. Furthermore there is an interestingly dominant minimum of the early wave, visible even in plots for higher times.

Using a $u(x)$-plot with five time steps for improved accuracy found in appendix D, the propagation speeds are calculated as

$$v_t = (1.705 \pm 0.11)\,\mathrm{mm}/\mu\mathrm{s} \tag{59}$$

$$v_l = (5.00 \pm 0.10)\,\mathrm{mm}/\mu\mathrm{s} \tag{60}$$

With the errors determined by the standard deviation. These values are slower than those at 50 kHz, consistent with dispersive behavior. In figure 20 a comparison with theoretical Lamb wave dispersion in a plate is illustrated.

This figure shows, that the transverse wave speeds align reasonably well with theoretical expectations. However, the longitudinal wave speeds are lower than theoretically expected for the glass plate. The spherical shell geometry is not expected to have the same dispersive behavior as the plate, but it should be similar, which is observed.
The final analysis considers the $u(t)$ curves for two probes along the inner side of the glass sphere, shown in figure 21.

Again, the propagation of both modes is observed, with the amplitude of the early wave being significantly smaller, than the amplitude of the late wave. The attenuation of the wave again is visible clearly in the reduction of the amplitude measured at the later probe. The simulations confirm the presence of two wave modes in both 50 kHz and 20 kHz cases. Fast and weak longitudinal waves, and slower, stronger transverse waves. The measured propagation speeds matched closely with the AMADEUS measurements, confirming the simulations to form a reliable basis for correcting errors in the KM3NeT positioning system.

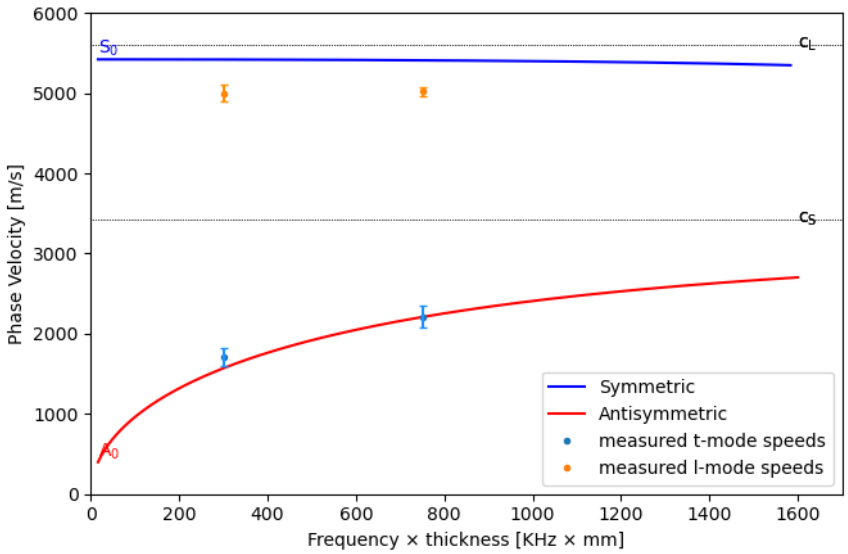

Figure 20: Theoretical dispersion curves and measured speeds plotted. The observed longitudinal wave speeds are lower than expected for the plate.

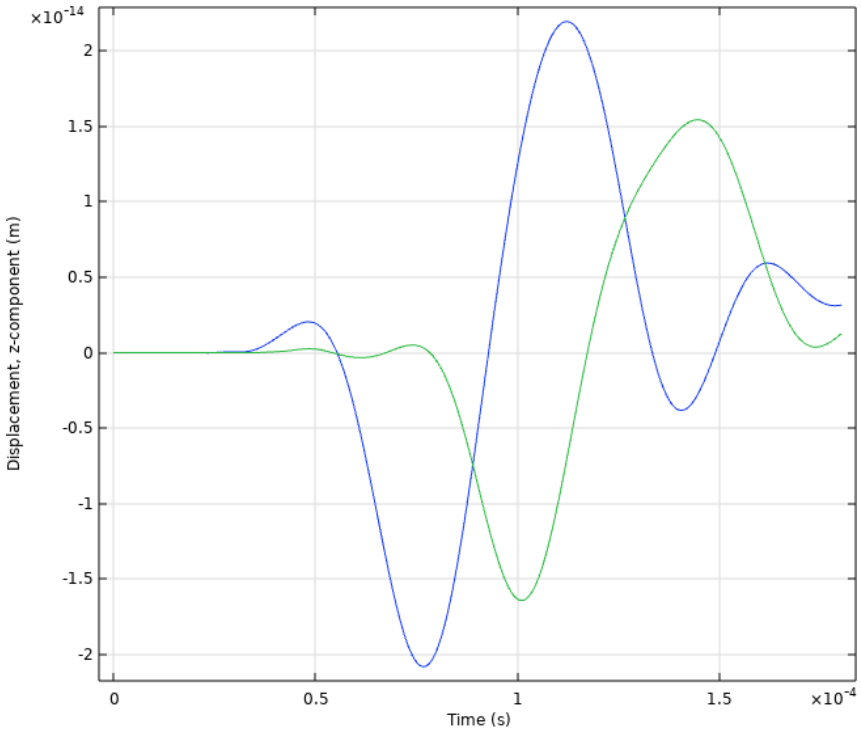

Figure 21: $u(t)$-plots for the probes located 158 mm (blue) and 210 mm (green) away from the POI.

6 Summary and conclusions

The acoustic positioning system of the KM3NeT neutrino telescope is subject to systematic uncertainties, one of which arises from the simplifying assumption that acoustic signals propagate exclusively through water. However, results from the modified AMADEUS experimental setup demonstrated that part of the acoustic signal couples into the glass shells of the digital optical modules (DOMs), forming Lamb-like waves. This effect introduces uncertainties in the expected arrival times not accounted for in the original system design. With experimental analysis a correction for the positioning system of ANTARES was derived, however, this experiment performed no analysis on KM3NeT signals. To address this experimental gap, and asses the feasibility of FEM simulations for modeling such effects, a series of simulations with increasing complexity were conducted.
The initial simulation employed a simple geometry of a thin glass plate, to evaluate the ability of FEM to capture the formation of Lamb waves. The results matched the theoretically derived dispersion relation, confirming the suitability of this method.
Subsequently, a more realistic geometry representing a DOM glass shell in a simplified surrounding medium was analyzed. The water domain was modeled as a solid, plastic material, to simplify the simulation. Using an excitation signal at 50 kHz, the simulation reproduced measurements of the AMADEUS experiment, validating the simulation setup. To extend the analysis to frequencies relevant for KM3NeT, the simulation was repeated with a 20 kHz signal. From these results, new propagation speeds were extracted and an updated dispersion plot for both DOM simulations was generated. The resulting speeds can inform corrections to the KM3NeT positioning algorithm by accounting for the different arrival times.

Overall, the study demonstrated the practicality of FEM for the modeling of elastic waves, providing a resource efficient alternative to experimental set ups. While the current model simplifies the fluid-solid interaction, the measured propagation speeds of the 20 kHz simulation already offer practical insights on the systematic error of the KM3NeT positioning system. Future work, building upon this study, should incorporate fluid-structure interaction to further refine the corrections and decrease the systematic positioning error.

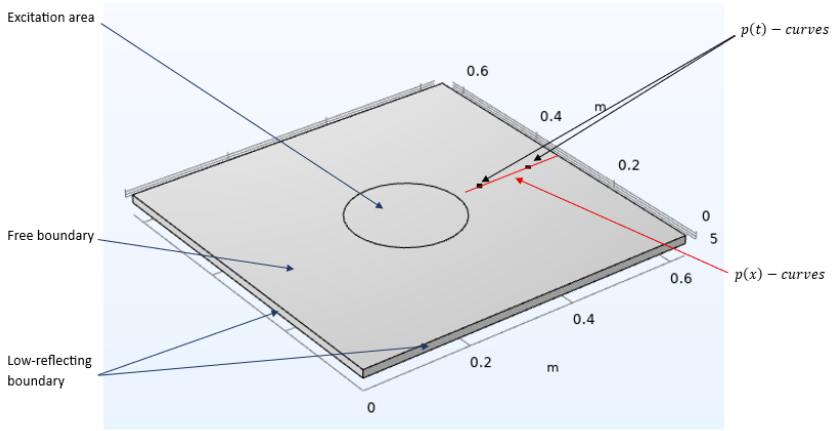

Figure 22: The first constructed plate model. Boundary conditions and graph acquisition is marked by the arrows.

A Simulation history

This appendix contains the different models that were created to analyze the impact of different simulation parameters on the results. These models all had problems, but are still broadly described to avoid running into known issues again, if there is any further analysis conducted on this topic. In table 1 a short summary of the plate model evolution is given.

A.1 Glass Plate

First model

The first plate model was composed of a single 15 mm thick plate made from VITROVEX glass with side lengths $d = 0.63\,\mathrm{m}$. On the top side there was a central, circular excitation area with a radius of $r_e = 100\,\mathrm{mm}$. Two points were defined, also on the top side of the plate as the point probes, as seen in figure 22. The boundaries are defined to be low reflecting on all sideward faces and free on the top and bottom sides.

the utilized signal was like the signal described in refsection3, apart of the spatial gaussian window. Meshing was also as fine as already described. The results of this simulation were acquired for the same time window as all the following models. In this stage, the pressure graphs were studied, which proved to be more prone to simulation errors and did not show the formation of lamb waves. In the pressure plots no lamb wave propagation could be properly observed. This was most likely due to a sharp pressure fall of at the rim of the excitation area as there was no spatial gaussian pressure modulation. The direct pressure excitation at one side of the glass plate, also does not represent the analyzed scenario properly as in AMADEUS the arrival of plane acoustic waves, propagating through water is studied as the excitation signal of the lamb wave. Also we will see that the displacement are a more accurate representation of the AMADEUS measurements.

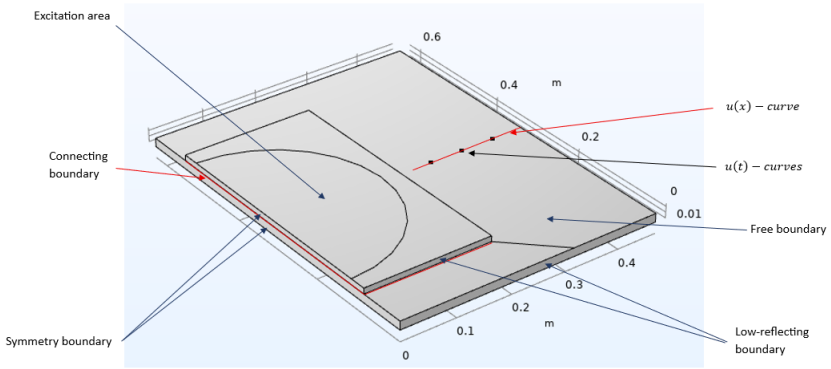

Figure 23: Figure of the two plate model with the probes and cut line object not covered. In the figure, the blue arrows represent boundary conditions, the red connecting boundary is the whole face touching the bottom plate.

Optimization 1

The first major change in the second attempt is the implementation of symmetry boundaries to reduce necessary computational power as well as reducing file sizes. For this the plate was cut in half and the condition was applied. This was the only change before re-running the simulation to produce the same results as before, proving the symmetry boundary condition to be a reliable tool. The signal was also modified with the spatial gaussian window, as described in sec3. With the new signal the sharp pressure cut-offs were not further observed in the resulting curves. The pressure plots still showed no formation of lamb waves. This was due to the other problems described in refpar1 of this simulation not being an accurate representation of the experimental situation, which is why from now on the displacement curves were generated using the *Compute Displacement* function of the Elastic Waves module. For this model, even these graphs did not show the clear formation of lamb waves. This could only be fixed with a change in utilized geometry.

Second model

The second model was composed of the half, glass plate as described before, with a second plate made of plastic stacked atop it. This plate was introduced, to simulate the wave propagating through water first. Both plates were defined as different domains, with an *Identity Boundary Pair* condition at the connecting boundaries. The excitation area was moved to the top side of the plastic, the point probes were not moved. The $u(x)$-plot data acquisition line also stayed on the top side of the glass plate. This proved to be problematic as the data at the boundary in between the plates was prone to simulation-based errors. In fact there was no observation of lamb waves using this setup. To fix this issue another model was created, in which the size of the plastic plate was reduced, to no longer cover the probes and the cut line object, as seen in figure 23.

In the resulting curves different mode speeds of lamb waves propagating could be observed, although for larger times the displacement seemed to diverge. To isolate the

problems leading to this effect, the different test simulations were run. First, the signal shape was changed to an single gaussian pulse, with a width of $\sigma_{gauss} = \frac{1}{2}T_{sin}$, with T_{sin} being the oscillation period of the 50kHz signal. With this excitation, the problem of diverging displacement for larger times could still be seen in the resulting curves. The sinusoidal signal is utilized for further simulations.

Third model

This model again, consists of two plates of the same size stacked on top of each other. This time the data acquisition happens at the bottom side of the glass plate. This is already quite similar to the final version of the plate model, with the major difference being that the excitation area has a much larger area of $r_e = 200\,\text{mm}$. The problem remains the same, so the next attempt is made, with an excitation area of $r_e = 100\,\text{mm}$ this was a step in the right direction, as results were more promising but wave speeds could not be measured as good as in the second model.

Solid Mechanics module

The *Solid Mechanics (solid)* module could theoretically also grant interesting insights on the acoustic behavior of the plates. This is because it directly solves for the displacement field as a dependent variable. A boundary load can still be applied and the rest of the setup of the physics works similarly to the *Elastic Waves, Time Explicit (elte)* module. In the results no wave propagation could be observed. This is because this module normally is better suited for tasks such as mode analyses. The utilization of the Elastic Waves module is advantageous for simulating the time explicit lamb wave propagation. The following models are constructed with this module.
In the next simulation attempt all outer boundaries, except the symmetry boundaries, were set to low-reflecting, to reduce interferences with reflected waves in the plate. The results showed the propagation of lamb waves, although they were strongly dampened across the bottom face, which is due to the boundary condition. This change also was reverted, as the observation of lowly dampened lamb waves was the goal.

Fourth model

This model is constructed as the model before, with only a change in the geometry. This time, the plate width was increased to reduce interferences with reflections off the sides. The resulting curves were the same as before and this change was reverted. For the next try the meshing of the model was set-up to finer, with a maximum element size of $m = 8\,\text{mm}$. This simulation took a lot more time to run and the results had better resolution along the curves, although the qualitative progression was not as expected from the AMADEUS results.

Final model

The next attempts were made with the setup of the third model, with only the excitation are decreased further. This time the radius was $r_e = 10\,\text{mm}$. The results showed promising lamb wave progression, but were quite noisy with reflections and, for higher

times, with numerical errors. For the next attempt the radius was increased to $r_e = 40\,\mathrm{mm}$ which is about half the expected wavelengths of the S_0 mode $\lambda_{ex} = \frac{5000\,\mathrm{m/s}}{50000\,\mathrm{hz}} = 100\,\mathrm{mm}$. The results showed nearly undisturbed lamb waves for time periods of $t = 60\,\mu\mathrm{s}$ as well as expected dispersion for simulations of of plates with different thicknesses. This model was utilized to study the wave behavior in the plate.

Table 1: Summary of FEM Simulation Model Evolution of the plate model

Model	**Key Features**	**Modifications**	**Results / Observations**
1 (Initial)	Single glass plate, $r_e = 100\,\text{mm}$, top pressure excitation	No spatial Gaussian window, direct pressure excitation	No Lamb waves, edge artifacts, inaccurate representation of AMADEUS
Optimization 1	Half-plate (symmetry BC), spatial Gaussian signal added	Applied symmetry, better signal shape	Still no Lamb waves; pressure plots insufficient; switched to displacement plots
2	Two plates (plastic on glass), Identity boundary condition	Plastic plate simulates water; excitation moved to plastic	No clear waves due to probe placement; boundary interface issues
2 (revised)	Same geometry, plastic size reduced	Plastic avoided probe region	Lamb modes visible, but displacement diverged at longer times
Pulse test	Same as above	Used single Gaussian pulse ($\sigma = \frac{1}{2}T$)	Divergence persisted; sinusoid used for further studies
3	Two plates, excitation $r_e = 200\,\text{mm}$, probes at bottom glass	Reduced r_e to 100 mm	Waveform improved but wave speed harder to measure
Solid Mechanics	Solved displacement directly	Switched to Solid Mechanics module	No wave propagation observed; not suitable for time-dependent Lamb wave modeling
Boundary test	Low-reflecting BC on all except symmetry	Damped reflections	Over-damped wave propagation; reverted
4	Increased plate width	Reduced edge reflections	No significant improvement; reverted
4 (refined)	Same geometry, finer mesh ($h = 8\,\text{mm}$)	Finer spatial resolution	Better numerical accuracy but no qualitative gain
Final	Two plates, $r_e = 40\,\text{mm}$, sinusoidal excitation	Smaller excitation area ($\approx$ half-wavelength)	Clear Lamb waves up to 60 µs, dispersion visible; used for final study

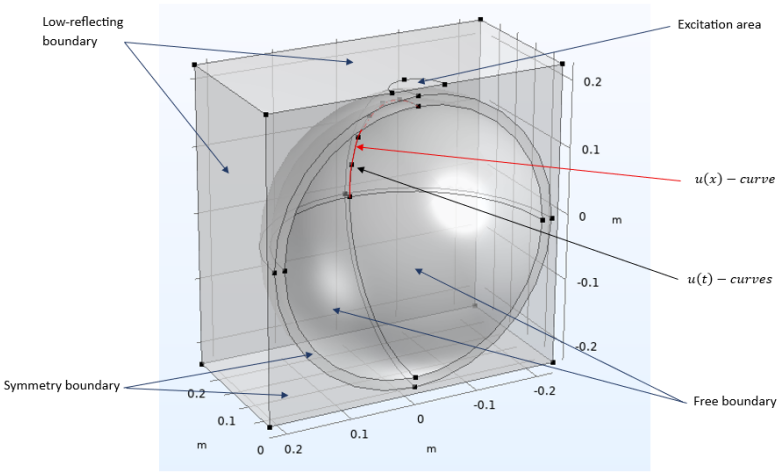

Figure 24: The first DOM-model. The blue arrows represent boundary conditions, the red and black arrows show the data acquisition line/points. The connecting boundary is the outer surface of the DOM touching the inner spherical surface of the block.

A.2 DOM geometry

First model

The first DOM model implemented a lot of properties from the plate simulation, as it was a well working basis. The main difference is the geometry which is now an glass spherical shell with a thickness of 15 mm embedded into a plastic cube with a densitiy of $\rho_{plast} = 0.91 \frac{\mathrm{g}}{\mathrm{cm}^3}$, simulating the ambient water. The circular excitation area is centrally located on the top side of the block with a radius of $r_e = 40\,\mathrm{mm}$. The problem is cut in half, making use of the Symmetry boundary condition. Data acquisition points are located across the inner surface of the spherical shell in the upper half. The $u(x)$-plots are generated across a line segment across the inner side of the spherical shell in the upper half as seen in 24.

In this simulation both the $u(t)$ and $u(x)$ displacement plots showed promising results. The two different propagation modes could be clearly observed and the speeds measured. As in AMADEUS the signal source is much farther away, the radius of the excitation area was further increased to $r_e = 100\,\mathrm{mm}$, to come closer to the plane wave approximation. The results were of similar quality so that the final change could be applied.

Final model

This model consists of the same geometry as before, with only the excitation area changed. This time the whole upper surface of the plastic block is excited with the same amplitude across the surface, meaning there is no more spatial gaussian modulation of the signal. This is the most accurate approximation of plane waves propagating through the plastic. As the results are an accurate depiction of AMADEUS measurements, this is the utilized setup for signal speed analysis.

B Modeling instructions

This appendix contains exact modeling instructions of the utilized models. All simulations were made and run in COMSOL Multiphysics 6.3, with the Physics module Elestic Waves, Time Explicit (elte) installed.

B.1 Glass plate

From the **File** menu, choose **New**.

New

1. In the **New** window click **Model Wizard**.
2. In the **Select Space Dimension** section click **3D**.
3. In the **Select Physics** interface open the **Acoustics** tab and then the **Elastic Waves** tab and select the module **Elastic Waves, Time explicit (elte)**.
4. Click **Add**.
5. Click **Study**.
6. Open the **General Studies** tab and click **Time Dependent**.
7. Select **Done** at the bottom of the menu.

Global Definitions

1. Open the **Global definitions** tab.
2. Click on **Parameters 1**.
3. Enter the following parameters:

Parameters

Name	Expression	Value	Description
p_w	0.63[m]	0.63 m	Width of the Plate
p_h	15[mm]	0.015 m	Height of the glass plate
r0	0.02[m]	0.02 m	Radius of spatial gaussian envelope
y0	0.315[m]	0.315 m	Center of spatial gaussian envelope
x0	0[m]	0 m	Center of spatial gaussian envelope
A	0.5[mPa]	5E-4 Pa	Amplitude of the Signal
f0	50[kHz]	50000 Hz	Frequency of the Signal
td	40[us]	4E-5 s	Delay of the Signal
sigma	20e-6[s]	2E-5 s	Width of time-dependent gaussian envelope
lambda	15e-6[s]	1.5E-5 s	Slope of the timing window
t0	10[ns]	1E-8 s	Start time of the Signal
t1	60[us]	6E-5 s	End time of the Signal
p_h_plast	10[mm]	0.01 m	Height of the plastic plate

4. In the Label field enter **Model Parameters**

Geometry

1. Click **Geometry 1**.
2. In the Label section enter **System**.
3. Right click **System** and click **Block**.
4. In the Label section enter **Plate Glass.**

5. Enter the following sizes in the **Size and Shape** section:

6. Right click **System** and click **More Primitives** and then **Point**.
7. In the Label section enter **Probe1**.
8. Enter the following values in the **Point** section:

9. Repeat steps 6. through 8. six more times increasing the label number by 1 as well as the x-coordinate by 60mm each time.
10. Right click **System** and click **Block**.
11. In the Label section enter **Plate Plastic**.
12. Enter the following values in the **Size and Shape** section:

13. Enter the following values in the **Position** section:

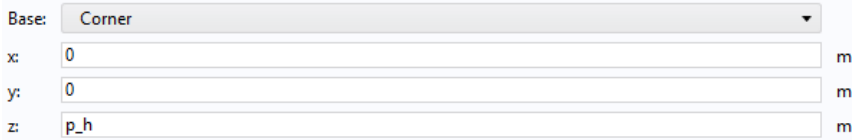

14. Right click **System** and click **Work Plane**.
15. In the **z-coordinate** section type **p_h+p_h_plastic**.
16. Open the **Work Plane 1** tab.
17. Right click **Plane Geometry** and click **Circle**.
18. In the sections **Size and Shape**, **Position** and **Rotation Angle** enter the following values:

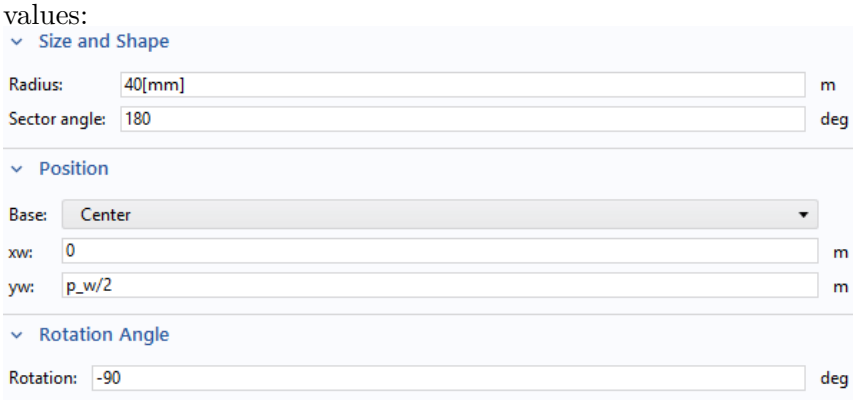

19. Right click **System** and click **Booleans and Partitions** and then **Union**.
20. Select the plastic plate and the work plane as input objects by clicking on them in the 3D view.
21. Right click **System** and click **Booleans and Partitions** and then **Union**.
22. Select the glass plate and all points as input objects by clicking on them in the 3D view.

23. Click on **Form Union**.
24. In the **Form Union/Assembly** section under action select **Form an assembly**.

Definitions

1. Right click the **Definitions** tab and click on **Probes** then **Point Probe**.
2. In the **Source Selection** section choose manual and remove all points from the selection by clicking on the selection and pressing delete on the keyboard.
3. Select the point **Probe1** in the 3D-view.
4. In the **Expression** section type **elte.uz** as the expression.
5. Repeat steps 1. through 4. for the remaining probes.
6. Right click the **Definitions** tab and click on **Pairs** then select **Identity Boundary Pair**.
7. Select the **Source Boundaries**, in this case the side of the plastic plate touching the glass plate in 3D view. To click this side in 3D-view it is recommended to use the **Click and Hide** tool in the Graphics interface and hiding the top side of the plastic. Before selecting the underside as the source boundary the tool has to be manually disabled by clicking again.
8. Toggle the selection to the **Destination Boundaries** by clicking the switch button.
9. Select the top side of the glass plate, again using the **Click and Hide** tool.
10. Click **System** and then **Build All** in the settings section.

Materials

1. Right click the **Materials** tab.
2. Click **Blank Material**
3. Select the bottom Plate in 3D-view.
4. In the Label field type **glass**.
5. In the **Material Contents** sections enter the following values:

Material Contents

Property	Variable	Value	Unit	Property group
Density	rho	2.23[g/cm^3]	kg/m³	Basic
Young's modulus	E	63[GPa]	Pa	Young's modulus and Poisson's ratio
Poisson's ratio	nu	0.2	1	Young's modulus and Poisson's ratio

6. Right click the **Materials** tab.
7. Click **Blank Material**
8. Select the top Plate in 3D-view.
9. In the Label field type **plastic**.
10. In the **Material Contents** section enter the following values:

Material Contents

Property	Variable	Value	Unit	Property group
Density	rho	0.91[g/cm^3]	kg/m³	Basic
Young's modulus	E	1.08[GPa]	Pa	Young's modulus and Poisson's ratio
Poisson's ratio	nu	0.15	1	Young's modulus and Poisson's ratio

Physics

1. Under **Elastic Waves, Time Explicit (elte)**, right click on **Elastic Waves, Time Explicit Model 1** and select **Compute Displacement**.
2. Select only the bottom plate in 3D-view.
3. Right click **Elastic Waves, Time Explicit (elte)** and select **Boundary Load**.
4. Select the semi-circular area in the 3D-view.
5. Under the section **Force** select the Load type **Force per area** and enter the following expression:

0	x
0	y
A * cos(2*pi*f0*(t - td)) * exp(-((t - td)^2)/(2*sigma^2)) * (1 - 1/(exp((t - t0)/lambda) + 1)) * (1/(exp((t - t1)/lambda) + 1)) * exp(-((x-x0)^2 + (y-y0)^2) / r0^2)	z

6. Right click **Elastic Waves, Time Explicit (elte)** and click on **Symmetry**.
7. Select the sideward faces next to the semicircular area of top and bottom plate in the 3D-view.

8. Right click **Elastic Waves, Time Explicit (elte)** and click on **Low-Reflecting Boundary**.
9. Select the remaining sideward faces in the 3D-view.

Mesh

1. Right click **Mesh 1** and select **Free Tetrahedral**.
2. Click on **Size 1** and in the **Element Size** section click **Custom**.
3. In the **Maximum element size** field type **16[mm]**.
4. In the **Minimum element size** field type **6[mm]**.
5. Click **Build All**.

Study

1. Click on **Step 1: Time Dependent**.
2. In the **Study Settings** section locate the **Output times** field and enter **range(0,5.0e-7,1.5e-4)**.
3. Click on **Compute**.
4. Wait for the simulation to finish computing, which might take up to 3 hours depending on utilized hardware.

Results

1. In the **Results** tab right click on **Datasets** and select **Cut Line 3D**.
2. In the **Line Data** section enter the following values:

	x:	y:	z:	
Point 1:	235[mm]	0.315	0	m
Point 2:	3*p_w/4+10[cm]	0.315	0	m

3. Right click the **Results** tab and select **1D Plot Group**.
4. In the label section enter **Signal**.

5. Right click **Signal** and select **Global**.
6. In the section **y-Axis Data** enter the signal expression from before into the table.
7. Right click the **Results** tab and select **1D Plot Group**.
8. In the label section enter **u(x)**.
9. Right click **u(x)** and select **Line Graph**.
10. In the **Data** section select **Cut Line 3D 1** as the dataset.
11. Still in the **Data** section select **From List** for the Time selection. The times for which the plot is generated can be selected from the list. Hold the control key to select multiple.
12. In the **y-Axis Data** section type **elte.uz**
13. In the **Legends** section tick the **Show legends** box.
14. The probe plots should be generated automatically. To Rename click on **Probe Plot Group 1** and in the label section enter **u(t)**.

B.2 DOM geometry

New

1. In the **New** window click **Model Wizard**.
2. In the **Select Space Dimension** section click **3D**.
3. In the **Select Physics** interface open the **Acoustics** tab and then the **Elastic Waves** tab and select the module **Elastic Waves, Time explicit (elte)**.
4. Click **Add**.
5. Click **Study**.
6. Open the **General Studies** tab and click **Time Dependent**.
7. Select **Done** at the bottom of the menu.

Global Definitions

1. Open the **Global definitions** tab.
2. Click on **Parameters 1**.
3. Enter the following parameters:

Name	Expression	Value	Description
r_o	(432/2)[mm]	0.216 m	Radius of the outer sphere
r_i	r_o-15[mm]	0.201 m	Radius of the inner sphere
A	5[mPa]	0.005 Pa	Amplitude of the signal
f0	50[kHz]	50000 Hz	Frequency of the signal
td	50[us]	5E-5 s	Delay of the signal
sigma	20e-6[s]	2E-5 s	width of time gaussian envelope
lambda	15e-6[s]	1.5E-5 s	Slope of the window function
t0	10[ns]	1E-8 s	Start of the signal
t1	60[us]	6E-5 s	End of the signal

4. In the Label field enter **Model Parameters**

Geometry

1. Click **Geometry 1**.
2. In the Label section enter **System**.

3. Right click **System** and click **Sphere**.
4. In the Label section enter **Outer Sphere**.
5. Enter the following sizes in the **Size and Shape** section:

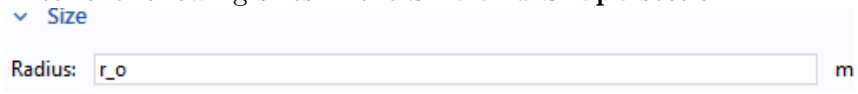

6. Right click **System** and click **Block**.
7. In the Label section enter **Plastic Block**.
8. Enter the following sizes in the **Size and Shape** section:

9. In the **Position** section for **Base** select **Center**.
10. Right click **System** and click **Booleans and Partitions** **Difference**.
11. In the **Difference** section select the plastic block in 3D-view as the Objects to add.
12. Toggle the selection to Objects to subtract by clicking the switch button and select the outer sphere for **Objects to subtract**. To click the sphere in 3D-view it is recommended to use the **Click and Hide** tool in the Graphics interface and hiding a side of the plastic. Before selecting the sphere the tool has to be manually disabled by clicking again. For this model this tool is quite important.
13. Tic the boxes **Keep objects to subtract** and **Keep interior boundaries**.
14. Right click **System** and click **Sphere**.
15. In the Label section enter **Inner Sphere**.
16. Enter the following sizes in the **Size and Shape** section:

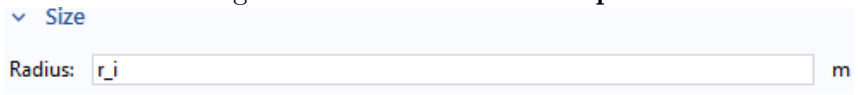

17. Right click **System** and click **Booleans and Partitions** **Difference**.
18. In the **Difference** section select the outer sphere in 3D-view as the Objects to add.
19. Toggle the selection to Objects to subtract by clicking the switch button and select the inner sphere for **Objects to subtract**.
20. Tic the box **Keep interior boundaries**.
21. Right click **System** and click **More Primitives** and then **Point**.
22. In the Label section enter **Probe1**.
23. Enter the following values in the **Point** section:

24. Repeat steps 6. through 8. six more times increasing the label number by 1 as well as decreasing the angle in the *sin* and *cos* by $\frac{\pi}{12}$ each time.
25. Right click **System** and click **Booleans and Partitions** and then **Union**.
26. Select the spherical shell and all the points by clicking on them in the 3D view.
27. Right click **System** and click **Booleans and Partitions** and then **Union**.
28. Select the plastic block by clicking on it in the 3D view.
29. Right click **System** and click **Work Plane**.

30. In the **Plane Definition** section for **Plane** select **yz-plane**.
31. Right click **System** and click **Booleans and Partitions** and then **Partition Objects**.
32. In the **Partition Objects** section select both unions as the objects to partition.
33. Select **Work Plane** from the **Partition with:** drop down menu. The correct work plane should be automatically selected.
34. Right click **System** and click **Delete Entities**.
35. in the **Entities or Objects to Delete** section select **Domain** in the **Geometric entity level:** selection.
36. Select the half of the block as well as the half of the spherical shell with negative x-coordinates, using the **Click and Hide** tool.
37. Click on **Form Union**.
38. In the **Form Union/Assembly** section under action select **Form an assembly**.

Definitions

1. Right click the **Definitions** tab and click on **Probes** then **Point Probe**.
2. In the **Source Selection** section choose manual and remove all points from the selection by clicking on the selection and pressing delete on the keyboard.
3. Select the point **Probe1** in the 3D-view.
4. In the **Expression** section type **elte.uz** as the expression.
5. Repeat steps 1. through 4. for the remaining probes.
6. Right click the **Definitions** tab and click on **Pairs** then select **Identity Boundary Pair**.
7. Select the **Source Boundaries**, in this case the inner 4 curved faces of the plastic block touching the glass sphere in 3D view. To click them in 3D-view it is recommended to use the **Click and Hide** tool in the Graphics interface and hiding the outer sides of the plastic block.
8. Toggle the selection to the **Destination Boundaries** by clicking the switch button.
9. Select the outer curved faces of the spherical shell, again using the **Click and Hide** tool.
10. Click **System** and then **Build All** in the settings section.

Materials

1. Right click the **Materials** tab.
2. Click **Blank Material**
3. Select the spherical shell in 3D-view.
4. In the Label field type **glass**.
5. In the **Material Contents** sections enter the following values:

Material Contents

Property	Variable	Value	Unit	Property group
Density	rho	2.23[g/cm^3]	kg/m³	Basic
Young's modulus	E	63[GPa]	Pa	Young's modulus and Poisson's ratio
Poisson's ratio	nu	0.2	1	Young's modulus and Poisson's ratio

6. Right click the **Materials** tab.

7. Click **Blank Material**
8. Select the block in 3D-view.
9. In the Label field type **plastic**.
10. In the **Material Contents** section enter the following values:

Material Contents

Property	Variable	Value	Unit	Property group
Density	rho	0.91[g/cm^3]	kg/m³	Basic
Young's modulus	E	1.08[GPa]	Pa	Young's modulus and Poisson's ratio
Poisson's ratio	nu	0.15	1	Young's modulus and Poisson's ratio

Physics

1. Under **Elastic Waves, Time Explicit (elte)**, right click on **Elastic Waves, Time Explicit Model 1** and select **Compute Displacement**.
2. Select only the spherical shell in 3D-view.
3. Right click **Elastic Waves, Time Explicit (elte)** and select **Boundary Load**.
4. Select the top face of the block in the 3D-view.
5. Under the section **Force** select the Load type **Force per area** and enter the following expression:

0	x	N/m²
0	y	
A * cos(2*pi*f0*(t - td)) * exp(-((t - td)^2)/(2*sigma^2)) * (1 - 1/(exp((t - t0)/lambda) + 1)) * (1/(exp((t - t1)/lambda) + 1))	z	

6. Right click **Elastic Waves, Time Explicit (elte)** and click on **Symmetry**.
7. Select all the sideward faces at $x = 0$ in the 3D-view.

8. Right click **Elastic Waves, Time Explicit (elte)** and click on **Low-Reflecting Boundary**.
9. Select the remaining outer sideward faces of the block in the 3D-view.

Mesh

1. Right click **Mesh 1** and select **Free Tetrahedral**.
2. Click on **Size 1** and in the **Element Size** section click **Custom**.
3. In the **Maximum element size** field type **16[mm]**.
4. In the **Minimum element size** field type **6[mm]**.
5. Click **Build All**.

Study

1. Click on **Step 1: Time Dependent**.
2. In the **Study Settings** section locate the **Output times** field and enter **range(0,5.0e-7,1.5e-4)**.
3. Click on **Compute**.
4. Wait for the simulation to finish computing, which might take up to 8 hours depending on utilized hardware.

Results

1. Right click the **Results** tab and select **1D Plot Group**.
2. In the label section enter **Signal**.
3. Right click **Signal** and select **Global**.
4. In the section **y-Axis Data** enter the signal expression from before into the table.
5. Right click the **Results** tab and select **1D Plot Group**.
6. In the label section enter **u(x)**.
7. In the **Data** section select **From table** in the **Time selection:** menu. The times for which the plot is generated can be selected from the list. Hold the control key to select multiple.
8. Right click **u(x)** and select **Line Graph**.
9. In the **Data** section select **from parent** as the dataset.
10. In the **Selection** section select **manual** for the Selection.
11. Still in the **Selection** section select all line segments across the inner side of the spherical shell at $y = 0$.
12. In the **y-Axis Data** section type **elte.uz**
13. In the **Legends** section tick the **Show legends** box.
14. The probe plots should be generated automatically. To Rename click on **Probe Plot Group 1** and in the label section enter **u(t)**.

C Material properties

This appendix contains the relevant material properties of the utilized materials. For the case of elastic wave propagation we need to know the density, Young's modulus and Poisson's ratio. For VITROVEX glass the properties are retrieved from [19]. They are:

$$\text{Specific gravity at } 25°\text{C:} \quad \rho = 2.23\,\text{g/cm}^3 \tag{61}$$
$$\text{Young's modulus:} \quad E = 63\,\text{GPa} \tag{62}$$
$$\text{Poisson's ratio:} \quad \nu = 0.20 \tag{63}$$

The plastic material utilized is low density polyethylene, with the Young's modulus retrieved from [17] and the density from [18]. There was no poisson's ratio specified in the source, which is why an arbitrary value, based on the poisson's ratio of similar polymers was utilized. The values utilized in the simulation for the plastic are:

$$\text{Specific gravity at } 25°\text{C:} \quad \rho = 0.91\,\text{g/cm}^3 \tag{64}$$
$$\text{Young's modulus:} \quad E = 1.08\,\text{GPa} \tag{65}$$
$$\text{Poisson's ratio:} \quad \nu = 0.15 \tag{66}$$

D Figures

This appendix contains additional figures utilized for measurements.

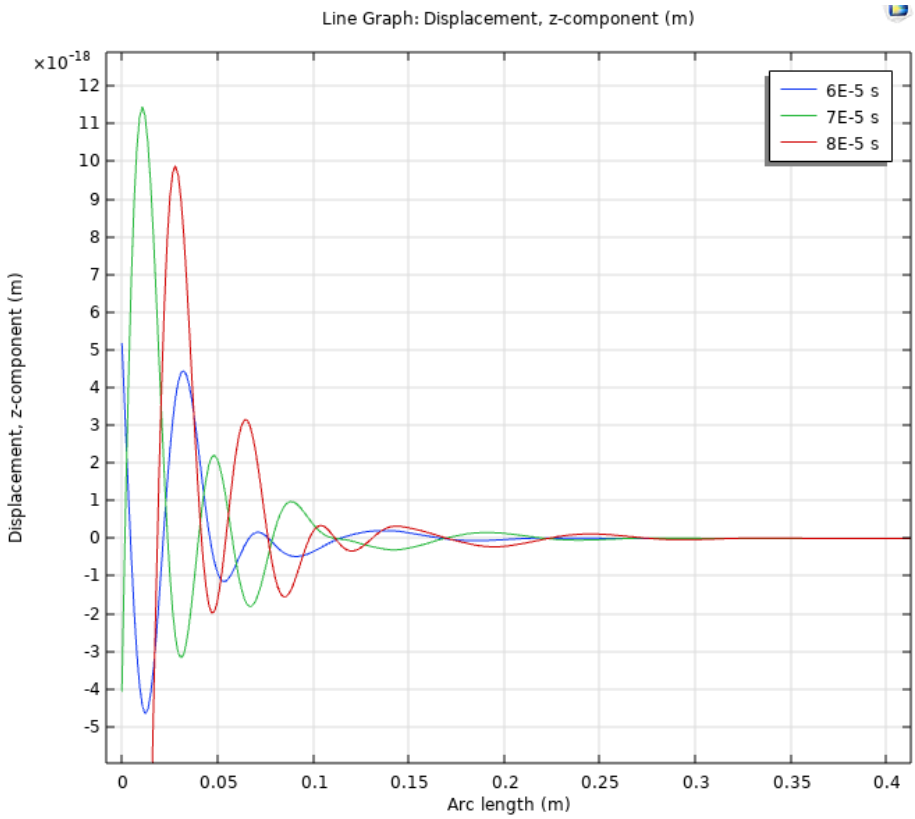

Figure 25: $u(x)$ curves for different times for the 7.5 mm plate. Both propagation modes are clearly observable

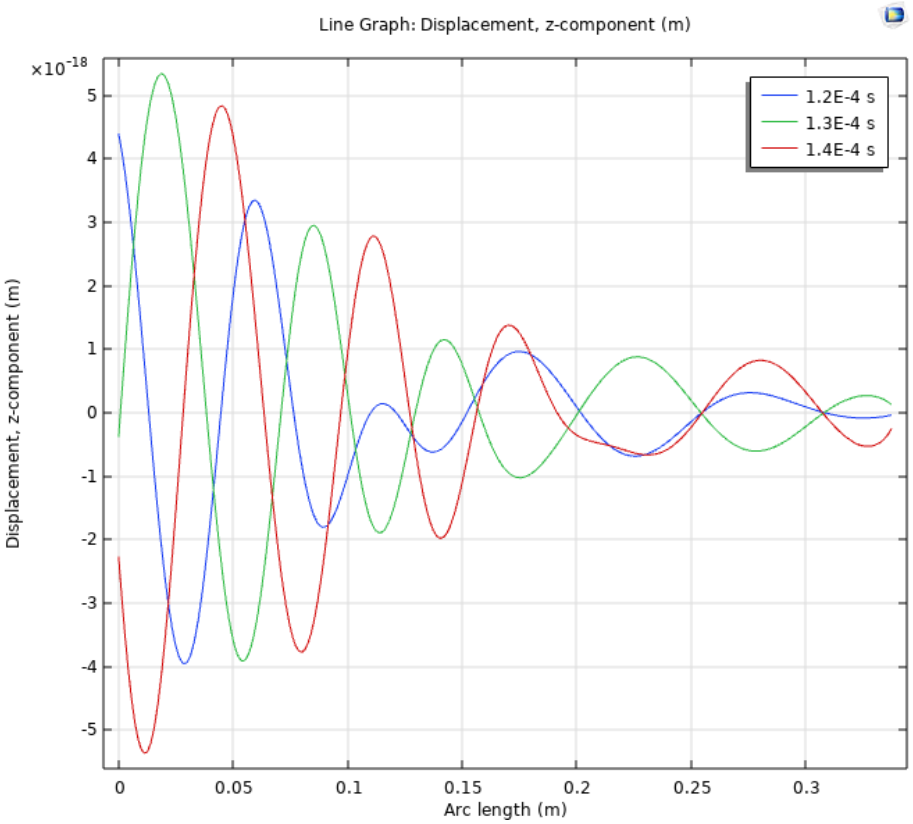

Figure 26: $u(x)$ curves for different times for the 30 mm plate. Both propagation modes are clearly observable

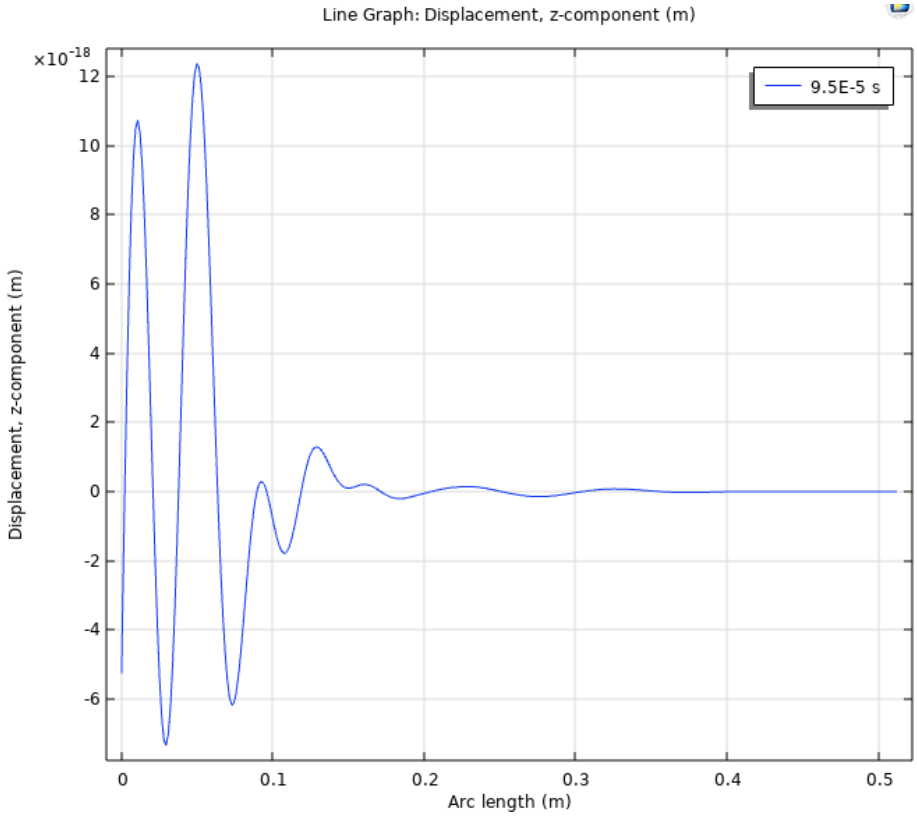

Figure 27: $u(x)$-plot of the 7.5 mm plate for a time, where the highest peak of the transverse wave is observed. The ratio is calculated with the highest peak value of the transverse wave and the highest peak value of the longitudinal wave.

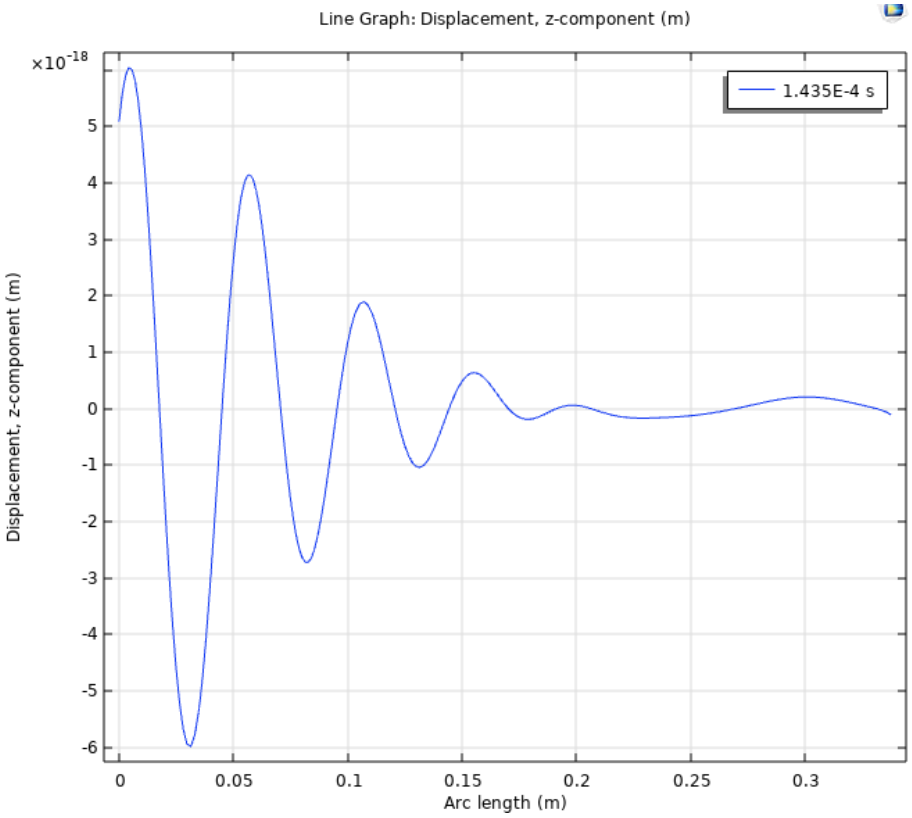

Figure 28: $u(x)$-plot of the 15 mm plate for a time, where the highest peak of the transverse wave is observed. The ratio is calculated with the highest peak value of the transverse wave and the highest peak value of the longitudinal wave.

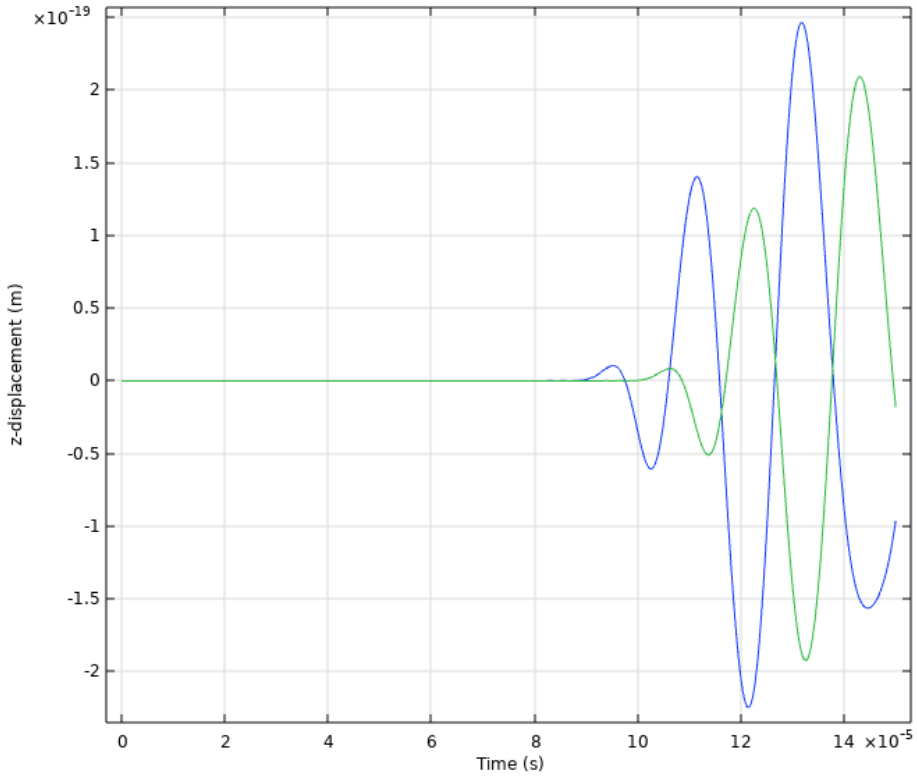

Figure 29: $u(t)$-plot of the 15 mm plate for probes at $x_1 = 475\,\text{mm}$ and $x_2 = 535\,\text{mm}$. It is used to calculate the amplitude decrease.

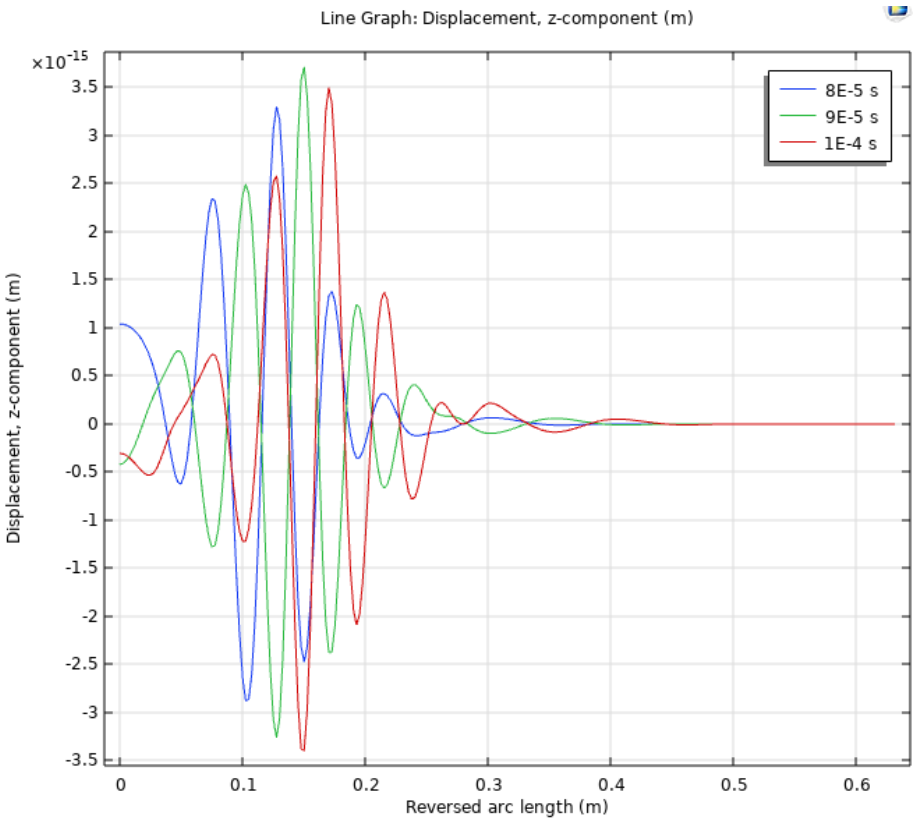

Figure 30: $u(x)$-plot of the 50 kHz DOM simulation for three different times. These peaks were utilized to determine the waves speeds.

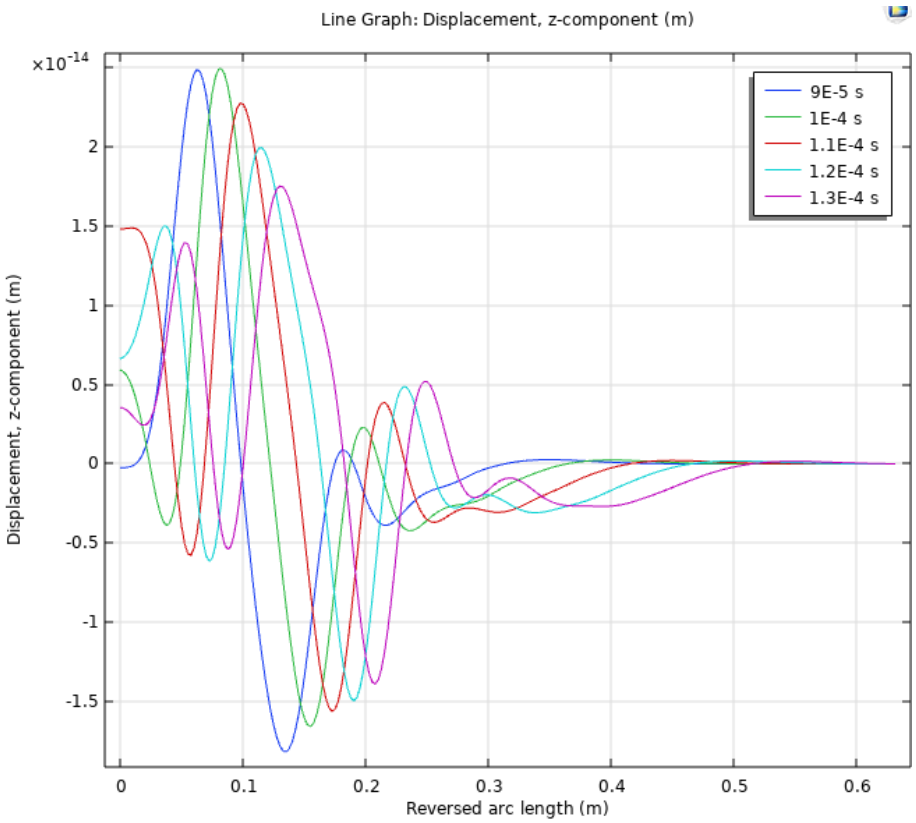

Figure 31: $u(x)$-plot of the 20 kHz DOM simulation for five different times. These peaks were utilized to determine the waves speeds.

References

[1] COMSOL. *Finite Element Method (FEM)*. COMSOL Multiphysics®. Retrieved June 17, 2025, from https://www.comsol.com/multiphysics/finite-element-method.

[2] Bathe, K.-J. (1996). *Finite Element Procedures*. Prentice Hall.

[3] COMSOL. (2020, August 6). Introduction to the Elastic Waves, Time Explicit Interface. Retrieved June 19, 2025, from https://www.comsol.com/blogs/introduction-to-the-elastic-waves-time-explicit-interface.

[4] Zienkiewicz, O. C., Taylor, R. L. (2005). The finite element method: Its basis and fundamentals (6th ed.). Elsevier Butterworth-Heinemann.

[5] Hughes, T. J. R. (2000). The finite element method: Linear static and dynamic finite element analysis. Dover Publications.

[6] Albert, A., Alves, S., Andre, M., Ardid, M., Ardid, S., Aubert, J.-J., Aublin, J., Baret, B., Basa, S., ... Zuniga, J. (2025). Acoustic positioning for deep sea neutrino telescopes with a system of piezo sensors integrated into glass spheres. Experimental Astronomy, 59, Article 6. https://doi.org/10.1007/s10686-024-09971-7.

[7] COMSOL. (2019). Definitions: Definitions Reference Manual (Version 5.5). COMSOL AB. Retrieved June 20, 2025, from https://doc.comsol.com/5.5/doc/com.comsol.help.comsol/comsol_ref_definitions.12.097.html.

[8] Albert, A., Alves, S., André, M., Ardid, M., Ardid, S., Aubert, J.-J., Aublin, J., Baret, B., Basa, S., Becherini, Y., ... Zúñiga, J. (2025). The ANTARES detector: Two decades of neutrino searches in the Mediterranean Sea. Physics Reports, 1121–1124, 1–46. https://doi.org/10.1016/j.physrep.2025.04.001.

[9] Adrián-Martínez, S., Ageron, M., Aiello, S., KM3NeT Collaboration. (2016). KM3NeT 2.0: Letter of intent for ARCA and ORCA. Journal of Physics G: Nuclear and Particle Physics, 43(8), 084001. https://doi.org/10.1088/0954-3899/43/8/084001.

[10] Adrián-Martínez, S., Ageron, M., Aguilar, J. A., Al Samarai, I., Albert, A., André, M., ... Zúñiga, J. (2012). The positioning system of the ANTARES Neutrino Telescope. Journal of Instrumentation, 7(08), T08002. https://doi.org/10.1088/1748-0221/7/08/T08002

[11] Amram, P., Anghinolfi, M., Anvar, S., Ardellier-Desages, F.E., Aslanides, E., Aubert, J.-J., Azoulay, R., Bailey, D., Basa, S., Battaglieri, M., Bellotti, R., Benhammou, Y., Bernard, F., Berthier, R., Bertin, V., Billault, M., Blaes, R., Bland, R.W.,Calzas, A. (2002). The ANTARES optical module. Nuclear Instruments and Methods in Physics Research Section A: Accelerators, Spectrometers, Detectors and Associated Equipment, 484(1–3), 369–383.

[12] KM3NeT Collaboration. (n.d.). About KM3NeT. KM3NeT. Retrieved June 25, 2025, fromhttps://www.KM3NeT.org/about-KM3NeT/

[13] Viola, S., Ardid, M., Bertin, V., Lahmann, R., Pellegrino, C., Riccobene, G., Saldaña, M., Sapienza, P., Simeone, F. (2015, July). Acoustic positioning system for KM3NeT. In Proceedings of the 34th International Cosmic Ray Conference (ICRC2015) (Vol. 34). KM3NeT Collaboration.

[14] Chen, C.-T., Millero, F. J. (1977). Speed of sound in seawater at high pressures. The Journal of the Acoustical Society of America, 62(5), 1129–1135.

[15] Rose, J. L. (2014). Ultrasonic guided waves in solid media (Chap. 6). Cambridge University Press.

[16] Achenbach, J. D. (1973). Wave propagation in elastic solids. North-Holland Publishing.

[17] Sonelastic®. (n.d.). Modulus of elasticity and Poisson's coefficient of polymeric materials [Data table]. Retrieved July 6, 2025, from Sonelastic® website: `https://www.sonelastic.com/en/fundamentals/tables-of-materials-properties/polymers.html`

[18] Linseis. (n.d.). Low density polyethylene (LDPE): A summary. Linseis. Retrieved July 6, 2025, from `https://www.linseis.com/en/wiki/low-density-polyethylene-ldpe-a-summary/`

[19] Nautilus Marine Service GmbH, VITROVEX instrumentation housings, Accessed on 6 March 2024, https://www.comm-tec.com/Docs/Brochure/Nautilus/200226

[20] Aguilar, J. A., Al Samarai, I., Albert, A., Anghinolfi, M., Anton, G., Anvar, S., Ardid, M., Assis Jesus, A. C., Astraatmadja, T., Aubert, J.-J., Auer, R., Barbarito, E., Baret, B., Basa, S., Bazzotti, M., Bertin, V., Biagi, S., Bigongiari, C., Bou-Cabo, M., Bouwhuis, M. C., ... Zúñiga, J. (2011). AMADEUS—The acoustic neutrino detection test system of the ANTARES deep-sea neutrino telescope. Nuclear Instruments and Methods in Physics Research Section A: Accelerators, Spectrometers, Detectors and Associated Equipment, 626–627, 128–143.